CANCER

Therapeutic targeting of CPSF3-dependent transcriptional termination in ovarian cancer

Peiye Shen[1,2] †, Kaiyan Ye[1,2]†, Huaijiang Xiang[3,4]†, Zhenfeng Zhang[1,2]†, Qinyang He[3,4], Xiao Zhang[3], Mei-Chun Cai[1,2], Junfei Chen[1,2], Yunheng Sun[1,2], Lifeng Lin[5], Chunting Qi[3], Meiying Zhang[1,2], Lydia W. T. Cheung[6], Tingyan Shi[5], Xia Yin[1,2], Ying Li[3], Wen Di[1,2]*, Rongyu Zang[5]*, Li Tan[3,7]*, Guanglei Zhuang[1,2]*

Transcriptional dysregulation is a recurring pathogenic hallmark and an emerging therapeutic vulnerability in ovarian cancer. Here, we demonstrated that ovarian cancer exhibited a unique dependency on the regulatory machinery of transcriptional termination, particularly, cleavage and polyadenylation specificity factor (CPSF) complex. Genetic abrogation of multiple CPSF subunits substantially hampered neoplastic cell viability, and we presented evidence that their indispensable roles converged on the endonuclease CPSF3. Mechanistically, CPSF perturbation resulted in lengthened 3′-untranslated regions, diminished intronic polyadenylation and widespread transcriptional readthrough, and consequently suppressed oncogenic pathways. Furthermore, we reported the development of specific CPSF3 inhibitors building upon the benzoxaborole scaffold, which exerted potent antitumor activity. Notably, CPSF3 blockade effectively exacerbated genomic instability by down-regulating DNA damage repair genes and thus acted in synergy with poly(adenosine 5'-diphosphate–ribose) polymerase inhibition. These findings establish CPSF3-dependent transcriptional termination as an exploitable driving mechanism of ovarian cancer and provide a promising class of boron-containing compounds for targeting transcription-addicted human malignancies.

INTRODUCTION

Ovarian cancer is often diagnosed at advanced stages and remains the most lethal gynecological malignancy (*1*, *2*). Over the past decades, debulking surgery and systemic chemotherapy are the mainstay treatments with a modest incremental improvement in survival rate (*3*). Recently, poly(adenosine 5′-diphosphate–ribose) polymerase (PARP) inhibitors that exploit synthetic lethality represent a major breakthrough but are limited to platinum-sensitive or homologous recombination-deficient patients (*4*). Emerging therapeutic modalities such as immune checkpoint agents have only achieved minimal success in clinical trials (*5*, *6*). Therefore, additional molecular regimens are urgently needed for better disease management. Nevertheless, the discovery of targeted drugs has been notoriously challenging because of lack of recurrent somatic mutations. Ovarian cancer is instead hallmarked by frequent copy number alterations, which promote tumorigenesis through dysregulated gene expression (*7*), thus implicating transcriptional addiction as a potentially actionable vulnerability (*8*).

Transcription cycle in eukaryotes comprises multiple discrete and sequential phases, i.e., initiation, elongation, and termination. Upon transcriptional initiation, RNA polymerase II is recruited to gene promoter and initiates nascent transcript synthesis. Following polymerase II pause release, RNA chain is productively generated via transcriptional elongation. Last, at the transcriptional termination stage when the consensus AAUAAA polyadenylation signal (PAS) is encountered, precursor mRNA (pre-mRNA) is cleaved and polyadenylated (*9*). These three progressive steps are meticulously controlled by corresponding protein complexes to ensure efficiency and accuracy (*10*). These regulatory programs also provide appealing opportunities to disrupt pathogenic transcription for therapeutic benefit in a spectrum of human cancers (*11*). For example, we and others have shown that pharmacological suppression of CDK7, a vital component of the transcriptional initiation apparatus, abrogates malignant growth by preferentially down-regulating oncogenes associated with superenhancers (*12*–*17*). In addition, bromodomain and extra-terminal (BET) protein, CDK9, or CDK12/CDK13 inhibitors undermine transcriptional elongation processivity and exhibit potent antineoplastic capacity (*18*–*24*). In stark contrast, the rationale and feasibility of targeting tumor dependence on transcriptional termination have been scarcely investigated.

Approximately 20 core factors have been identified to form four functional modules and carry out transcriptional termination in conjunction with other key elements, such as polyadenylate [poly (A)] polymerase and the symplekin scaffold protein (*25*, *26*). Specifically, CPSF (cleavage and polyadenylation specificity factor) binds to the hexanucleotide PAS and catalyzes pre-mRNA cleavage (*27*–*29*). Meanwhile, CstF (cleavage stimulation factor) recognizes G/U-rich sequences downstream of the PAS (*30*), whereas CFIIm (mammalian cleavage factor II) bridges CPSF and CFIm to contact the

[1]State Key Laboratory of Systems Medicine for Cancer, Department of Obstetrics and Gynecology, Shanghai Cancer Institute, Ren Ji Hospital, Shanghai Jiao Tong University School of Medicine, Shanghai, China. [2]Shanghai Key Laboratory of Gynecologic Oncology, Ren Ji Hospital, Shanghai Jiao Tong University School of Medicine, Shanghai, China. [3]Interdisciplinary Research Center on Biology and Chemistry, Shanghai Institute of Organic Chemistry, Chinese Academy of Sciences, Shanghai, China. [4]University of Chinese Academy of Sciences, Beijing, China. [5]Ovarian Cancer Program, Department of Gynecologic Oncology, Zhongshan Hospital, Fudan University, Shanghai, China. [6]School of Biomedical Sciences, Li Ka Shing Faculty of Medicine, The University of Hong Kong, Hong Kong, China. [7]State Key Laboratory of Chemical Biology, Shanghai Institute of Organic Chemistry, Chinese Academy of Sciences, Shanghai, China.
*Corresponding author. Email: zhuangguanglei@gmail.com (G.Z.); tanli@sioc.ac.cn (L.T.); zang.rongyu@zs-hospital.sh.cn (R.Z.); diwen163@163.com (W.D.)
†These authors contributed equally to this work.

upstream UGUA motif (*31*). Here, we systematically assessed ovarian cancer reliance on these macromolecular assemblies using CRISPR-Cas9 and pinpointed the indispensable roles of certain CPSF subunits that converged on the endonuclease CPSF3. A series of CPSF3 antagonists were developed on the basis of the benzoxaborole backbone and exerted pronounced antitumor activity. Notably, CPSF3 blockade significantly down-regulated DNA damage repair (DDR) genes and caused a "BRCAness" (a defect mimicking BReast CAncer gene loss) phenotype that conferred sensitivity to PARP inhibitors. Overall, these results established targeting CPSF3-dependent transcriptional termination as a feasible and valid therapeutic approach against otherwise intractable ovarian cancer.

RESULTS

Expression and dependence of CPSF subunits in ovarian cancer

Ovarian cancer pathogenesis has been increasingly linked to aberrant gene expression machinery operating in transformed cells, which can be leveraged for therapeutic purposes. To comprehensively delineate the resultant transcriptional addiction of ovarian cancer, we analyzed the fitness effects of diverse transcription–related components based on genome-scale CRISPR-Cas9 library screens from the Cancer Dependency Map (DepMap) portal. Most of 58 ovarian cancer cell lines displayed ubiquitous dependency on putative transcriptional regulators involved in initiation, elongation, and termination (fig. S1). Concentrating on the less appreciated role of transcriptional termination (Fig. 1A), we individually knocked out a selected list of 23 core factors using two separate single-guide RNA (sgRNA) sequences in three different models (OVCA420, OVCAR8, and OV-90). Notably, among the above-mentioned multiprotein functional modules including CPSF, CstF, CFIm, and CFIIm, genetic deletion of most CPSF subunits (Fig. 1B), particularly CPSF1, CPSF2, CPSF3, and WD repeat domain 33 (WDR33), consistently hampered cell viability as determined by colony growth assay (fig. S1B). These results were validated in six additional cell lines (SKOV3, COV362, PEO1, HEY, OVCA433, and SNU-251), demonstrating the broad essentiality of CPSF complex in ovarian cancer (Fig. 1C). Further supporting this notion, CPSF deficit in SKOV3 cells significantly impaired in vivo growth of intraperitoneal xenotransplants as monitored by bioluminescence imaging (Fig. 1D).

In line with their oncogenic potential, all CPSF subunits showed copy number gain in a subset of ovarian cancers from The Cancer Genome Atlas (TCGA) (fig. S2A). Droplet-based single-cell RNA sequencing (RNA-seq) on surgically resected neoplastic lesions from two treatment-naïve subjects uncovered that gene transcripts of CPSF constituents were disproportionally enriched in the tumor cell compartment (Fig. 1E), without evident discrepancy between matched primary and metastatic specimens according to transcriptomic profiling of a 118-patient cohort (fig. S2B). At the protein level, CPSF immunohistochemistry (Fig. 1F) on a tissue microarray containing 135 ovarian cancer samples (table S1) indicated predominantly positive staining (Fig. 1G), irrespective of disease stages (fig. S2C), or chemotherapy exposure (fig. S2D). We concluded that CPSF subunits were prominently expressed and largely indispensable in ovarian cancer.

The central role of CPSF3 endonuclease in ovarian cancer

The CPSF complex consisted of at least six interacting proteins including CPSF1, CPSF2, CPSF3, CPSF4, factor interacting with PAPOLA and CPSF1 (FIP1L1), and WDR33 (*32*). We found that the six CPSF subunits appeared to present dichotomous effects both in vitro (Fig. 1C) and in vivo (Fig. 1D), i.e., CPSF1, CPSF2, CPSF3, and WDR33, were distinctive from CPSF4 and FIP1L1 in terms of tumor promotion. These unexpected findings prompted us to interrogate their specific impact on ovarian cancer cell behavior. Using SKOV3 as a model system, flow cytometry analysis of cell cycle (fig. S3A) revealed that gene knockout of *CPSF1*, *CPSF2*, *CPSF3*, or *WDR33*, rather than *CPSF4* or *FIP1L1*, resulted in marked G_2-M arrest (Fig. 2A). Similar observations were made with the fluorescent ubiquitination–based cell cycle indicator (fig. S3B). In addition, EdU (5-ethynyl-2′-deoxyuridine) incorporation and annexin V/PI (propidium iodide) double staining assays supported that only *CPSF1*, *CPSF2*, *CPSF3*, or *WDR33* depletion impaired cell proliferation (Fig. 2B) and induced cell apoptosis (Fig. 2C), which was confirmed by IncuCyte live imaging (fig. S3C). Transmission electron microscopy unveiled abnormal polynucleolar structures upon *CPSF1*, *CPSF2*, *CPSF3*, or *WDR33* loss, in contrast to generally intact cell morphology in the absence of *CPSF4* or *FIP1L1* (Fig. 2D). Therefore, CPSF1, CPSF2, CPSF3, and WDR33, but not CPSF4 or FIP1L1, could impart proproliferative and prosurvival function to contribute to ovarian cancer aggressiveness.

The CPSF complex can be divided into two functional subcomplexes (Fig. 2E). The mPSF (mammalian polyadenylation specificity factor) subcomplex, constituted by CPSF1, WDR33, CPSF4, and FIP1L1, is necessary and sufficient for PAS recognition and polyadenylation (*32*). Specifically, CPSF1 functions as an essential scaffold, which organizes WDR33 and CPSF4 for high-affinity binding to the AAUAAA hexamer (*33*–*35*), while FIP1L1 recognizes adjacent U-rich sequence elements on the pre-mRNA and recruits poly (A) polymerase (*36*, *37*). Within the mCF (mammalian cleavage factor) subcomplex, CPSF3 is the endoribonuclease for catalyzing the cleavage reaction, and its structurally related CPSF2 is thought to assist this process (*28*, *29*, *38*). Recent evidence establishes that the CPSF1-WDR33 heterodimer serves as the organizational core of the whole machinery, whereas the conformation of interacting CPSF3-CPSF2 is relatively flexible (*39*). Hence, we reasoned that the comparable effects of CPSF1, CPSF2, CPSF3, and WDR33 ablation might be plausibly explained by their convergent influence on the endonucleolytic cleavage. CPSF1-WDR33 was coimmunoprecipitated with CPSF3-CPSF2, and the interaction between CPSF3 and CPSF2 seemed to be enhanced by CPSF1-WDR33 (Fig. 2F). As a matter of fact, *CPSF1*, *CPSF2*, or *WDR33* depletion, reminiscent of *CPSF3* knockout, invariably reduced CPSF3 levels in SKOV3, COV362, and OVCA420 cells (Fig. 2G), implying the presence of a stable protein complex. Consistent with the reportedly weak enzymatic activity of CPSF3 in isolation (*40*), exogenous overexpression only rescued the antitumor outcome produced by genetic deletion of *CPSF3*, but not *CPSF1*, *CPSF2*, or *WDR33* (Fig. 2H). On the basis of these results, we proposed that the endonuclease CPSF3 relied on proper CPSF complex assembly and played a central role in ovarian cancer.

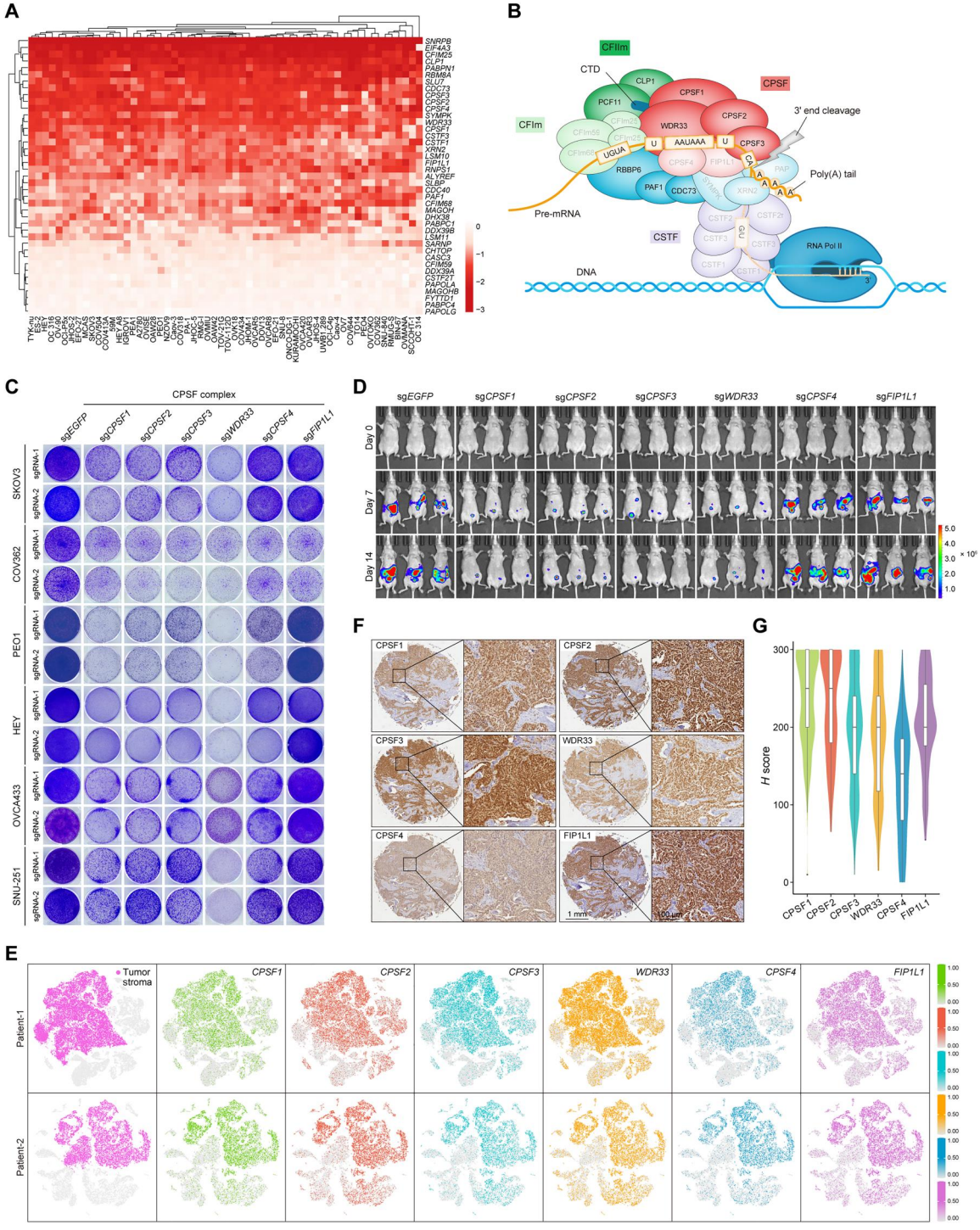

Fig. 1. Expression and dependence of CPSF subunits in ovarian cancer. (**A**) Heatmap of dependency scores for putative regulators of transcriptional termination in ovarian cancer cell lines (n = 58) from the DepMap project. (**B**) A schematic model of core factors involved in pre-mRNA cleavage and polyadenylation. The CPSF, CstF, CFIm, and CFIIm functional modules are shown in red, purple, aqua, and green, respectively. The subunits essential for cell viability based on the results of gene knockout are highlighted. (**C**) *CPSF1*, *CPSF2*, *CPSF3*, *WDR33*, *CPSF4*, or *FIP1L1* was knocked out in SKOV3, COV362, PEO1, HEY, OVCA433, and SNU-251 cells using CRISPR-Cas9 with two independent sgRNAs, and cell viability was assayed by crystal violet staining. (**D**) SKOV3 cells with or without CPSF subunits depletion were labeled with firefly luciferase and implanted intraperitoneally. Tumor growth in nude mice was monitored by bioluminescence imaging. (**E**) Ovarian cancer specimens from two patients were analyzed using single-cell RNA sequencing (RNA-seq). The *t*-distributed stochastic neighbor embedding plots show tumor and stroma cells and relative expression levels of *CPSF1*, *CPSF2*, *CPSF3*, *WDR33*, *CPSF4*, and *FIP1L1*. Each dot represents a single cell. (**F**) Representative immunohistochemical images of CPSF1, CPSF2, CPSF3, WDR33, CPSF4, and FIP1L1 staining in a tissue microarray containing 135 ovarian cancer samples. Scale bar, 1 mm. (**G**) Violin plots showing staining intensity of CPSF1, CPSF2, CPSF3, WDR33, CPSF4, and FIP1L1 in the ovarian cancer tissue microarray. The *H* score system was used for immunohistochemical quantification.

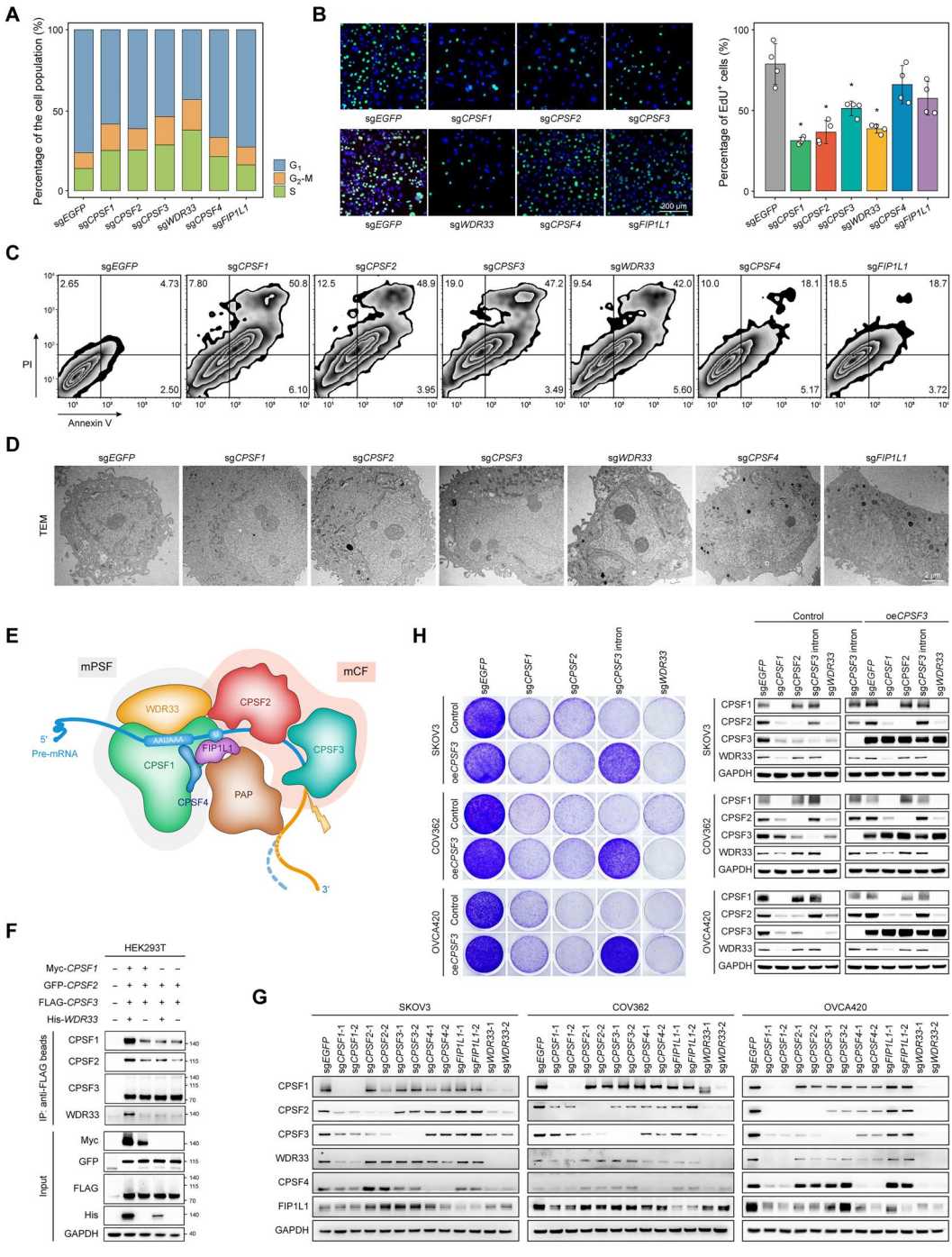

Fig. 2. The central role of CPSF3 endonuclease in ovarian cancer. (**A**) Cell cycle analysis by flow cytometry on SKOV3 cells with *CPSF1*, *CPSF2*, *CPSF3*, *WDR33*, *CPSF4*, or *FIP1L1* knockout. (**B**) EdU incorporation assay on SKOV3 cells with *CPSF1*, *CPSF2*, *CPSF3*, *WDR33*, *CPSF4*, or *FIP1L1* knockout. Cell nuclei were counterstained with 4′,6-diamidino-2-phenylindole (DAPI; blue). Quantification on the percentage of EdU-positive (green) cells is plotted as means ± SD ($n = 4$). *$P < 0.05$, analysis of variance (ANOVA) followed by Tukey's posttest. Scale bar, 200 μm. (**C**) Flow cytometric analysis of cell death using annexin V/PI double labeling in SKOV3 cells with *CPSF1*, *CPSF2*, *CPSF3*, *WDR33*, *CPSF4*, or *FIP1L1* knockout. (**D**) Representative transmission electron microscopy (TEM) images of SKOV3 cells with *CPSF1*, *CPSF2*, *CPSF3*, *WDR33*, *CPSF4*, or *FIP1L1* knockout. Scale bar, 2 μm. (**E**) A schematic model of core CPSF complex, which consists of mPSF and mCF subcomplex. The mPSF subcomplex, constituted by CPSF1, WDR33, CPSF4, and FIP1L1, is necessary and sufficient for PAS recognition and polyadenylation. CPSF2 and CPSF3 form the mCF subcomplex, which is responsible for catalyzing the cleavage reaction. CPSF1 and WDR33 interact with each other and act as a structural scaffold of the CPSF complex. (**F**) Myc-tagged *CPSF1*, green fluorescent protein (GFP)–tagged *CPSF2*, 3× FLAG-tagged *CPSF3*, or His-tagged *WDR33* was transfected into human embryonic kidney (HEK) 293T cells. CPSF3 was immunoprecipitated, and CPSF1, CPSF2, CPSF3, or WDR33 was analyzed by immunoblotting. IP, immunoprecipitation; GAPDH, glyceraldehyde-3-phosphate dehydrogenase. (**G**) *CPSF1*, *CPSF2*, *CPSF3*, *WDR33*, *CPSF4*, or *FIP1L1* was knocked out in SKOV3, COV362, and OVCA420 cells using CRISPR-Cas9 with two independent sgRNAs, and the indicated proteins were analyzed by immunoblotting. (**H**) *CPSF3* was overexpressed in SKOV3, COV362, and OVCA420 cells with *CPSF1*, *CPSF2*, *CPSF3*, or *WDR33* knockout, and the indicated proteins were analyzed by immunoblotting. Cell viability was assayed by crystal violet staining.

Altered pre-mRNA 3′-end processing and gene expression upon CPSF depletion

Focusing on CPSF1, CPSF2, CPSF3, and WDR33, we set out to explore the molecular mechanisms underlying CPSF dependency in ovarian cancer. Previous studies illuminated that unreleased chromatin-bound transcripts due to defective termination would trigger the formation of persistent RNA-DNA hybrids called R-loops and failure of pre-mRNA export driven by suppressors of the transcriptional defects of hpr1Δ by overexpression (THO) complex (*41*, *42*), both leading to transcription-replication conflict and consequent genomic instability. However, we found that CPSF-ablated SKOV3 cells did not exhibit an obvious escalation of nuclear R-loops detected by immunofluorescence staining (fig. S4A) or cleavage under targets and tagmentation profiling (fig. S4B) using

the S9.6 antibody nor did their growth repression become reversed by *THOC1* or *THOC2* codepletion (fig. S4C). In agreement with this observation, cell treatment with low dose of DNA polymerase inhibitor aphidicolin to relieve transcription-replication interference did not mitigate the antiproliferative action of CPSF knockout (fig. S4D). Likewise, CPSF loss was not associated with conspicuous genomic catastrophe involving dramatic changes of chromosome accessibility (fig. S4E) and copy number status (fig. S4F), as inferred by the assay for transposase-accessible chromatin by sequencing and whole-genome sequencing analysis, respectively. These data suggested that the compromised cell viability could not be attributed to the accumulation of detrimental RNA structures incited by dysfunctional termination.

On the other hand, CPSF interference may cause deviated pre-mRNA 3′-end processing, e.g., alternative cleavage and polyadenylation or even transcriptional readthrough. The resultant transcripts with different 3′ untranslated regions (UTRs) are considered to contribute to dysregulated gene expression by altering mRNA stability, translation efficiency, or cellular localization. To address this possibility, RNA-seq was conducted on SKOV3 cells edited by CRISPR-Cas9. In the absence of *CPSF1*, *CPSF2*, *CPSF3*, or *WDR33*, bioinformatics analysis of distal-to-proximal PAS switch using the DaPars method captured 163 to 466 genes with lengthened 3′UTR in comparison to 20 to 72 genes with shortened 3′UTR (Fig. 3A and tables S2 to S5). As two examples, *CFLAR* and *ALS2CL*, reportedly involved in cancer development (*43*, *44*), displayed increased RNA-seq read density within their 3′UTRs in response to CPSF disruption (fig. S5A). In more extreme scenarios, we noted diminished intronic polyadenylation (IpA) usage with the IPAFinder algorithm (Fig. 3B and tables S6 to S9), as illustrated by evident decrease in composite IpA of *DIDO1* and skipped IpA of *ZCCHC10* following CPSF knockout (fig. S5B), both linked to tumorigenesis (*45*, *46*). Furthermore, in keeping with the pivotal role of CPSF complex in pre-mRNA cleavage, individual manipulation of the four CPSF subunits yielded 1058 to 1755 readthrough transcripts beyond the annotated 3′UTR boundary (Fig. 3C and tables S10 to S13), including key ovarian cancer genes such as *PAX8* and *ARHGAP29* (fig. S5C) (*47*–*49*). Subsequently, we identified a considerable number of differentially expressed genes upon CPSF depletion (Fig. 3D and tables S14 to S17). Gene set enrichment analysis (GSEA) pinpointed uniformly suppressed oncogenic pathways related to cell metabolism, organelle biogenesis, and DNA repair (Fig. 3E), presumably accounting for the alleviated tumor aggressiveness observed earlier. In addition, there existed an overrepresentation of PAX8 gene signature in CPSF-modulated transcripts (Fig. 3F), implying the requirement of proper transcriptional termination for maintaining robust lineage–survival core regulatory circuitry. Notably, correlation matrix heatmaps highlighted that global events of alternative polyadenylation (APA) (fig. S5D), IpA (fig. S5E), transcriptional readthrough (fig. S5F), and differential gene expression (fig. S5G) were each significantly correlated in SKOV3 cells with genetic deletion of *CPSF1*, *CPSF2*, *CPSF3*, or *WDR33*. Collectively, these findings unequivocally demonstrated that CPSF perturbation substantially affected pre-mRNA 3′-end processing and gene expression in ovarian cancer.

Attenuated DDR upon CPSF depletion

A particularly intriguing observation from the RNA-seq study was the disproportional down-regulation of DDR genes once *CPSF1*, *CPSF2*, *CPSF3*, or *WDR33* was knocked out. Putative DDR genes showing aberrant events of APA (fig. S6A), IpA (fig. S6B), and transcriptional readthrough (fig. S6C) were also present. We further corroborated these results by performing GSEA with a well-curated 276-member gene set defined by TCGA (Fig. 4A) encompassing major DDR pathways (fig. S6D) (*50*). To probe the potential underpinnings of CPSF loss–related transcriptional changes, we surveyed a range of gene features. Notably, genes with larger sizes (Fig. 4B), longer coding sequences (Fig. 4C), higher exon numbers (Fig. 4D), or extra polyadenylation sites (Fig. 4E) tended to be more dramatically affected by CPSF disturbance. DDR genes fulfilled all the above criteria and were thus prone to CPSF ablation (fig. S7). Disrupted DDR gene expression had meaningful functional consequences to elicit genomic instability. Immunoblotting (Fig. 4F) and immunofluorescence (Fig. 4G) experiments detected the phosphorylated form of H2A histone family member X (γH2AX) aggregation in CPSF-depleted SKOV3 and COV362 cells, along with clearly increased tail moment in comet assays (Fig. 4H), indicating excessive accumulation of DNA double-strand breaks. Therefore, CPSF deficiency induced DNA damage through suppressing DDR gene expression.

Discovery of benzoxaborole-based CPSF3 inhibitors

On the basis of the above findings, we reasoned that the endonuclease CPSF3 might serve as a pharmacologically exploitable vulnerability in ovarian cancer. Initially, a series of benzoxaborole derivatives, inspired by previously reported microbicidal and parasiticidal agents targeting microbic and parasitic CPSF3 (*51*–*54*), were tested against SKOV3 cells at 3 μM, and none of them showed evident antitumor activity (fig. S8A). Recently, JTE-607 was proven to engage the large interfacial cavity of human CPSF3 and represented an unprecedented therapeutic modality in acute myeloid leukemia and Ewing's sarcoma (*55*). However, we found that JTE-607 at 3 μM had no detectable antineoplastic effect in ovarian cancer nor did its hybrids with the benzoxaborole moiety (fig. S8B). On the other hand, we noticed that a series of benzoxaboroles containing 7-propanamide and biphenyl modifications, e.g., compound **115**, were reported to have potent cytotoxic capacity with unknown mechanism of action (*56*). Molecular docking analysis based on CPSF3 and JTE-607 cocrystal structure [Protein Data Bank ID: 6M8Q] predicted that **115** was able to occupy the active site of CPSF3 endonuclease (Fig. 5A). Thus, we hypothesized that CPSF3 could be the intracellular target of **115** and analogs. In the predicted binding mode, **115** resided in CPSF3 with its 3-acetylphenyl group protruding toward the solvent phase. To further optimize **115**, we introduced more hydrophilic substituents to replace the 3-acetylphenyl group, aiming to reduce potential nonspecific hydrophobic interactions and improve drug solubility and bioavailability. Three new molecules (fig. S9A), namely, HQY426, HQY436, and XHJ1049, mirrored **115** to bind CPSF3 (Fig. 5A) and inhibited SKOV3 and COV362 cell viability, in contrast to HQY429, a control compound with different positions of morpholinyl group from HQY426 (Fig. 5B). Cellular thermal shift assays revealed that **115**, HQY426, HQY436, and XHJ1049 consistently stabilized endogenous CPSF3 in SKOV3 and COV362 cells (Fig. 5C), suggestive of direct engagement. To validate CPSF3 as an interacting substrate of our rationally designed inhibitors, we generated a photoaffinity labeling probe, XHJ1167, and its control probe, HQY54 (fig. S9B). Both XHJ1167 and HQY54 consisted of a photoreactive diazirine

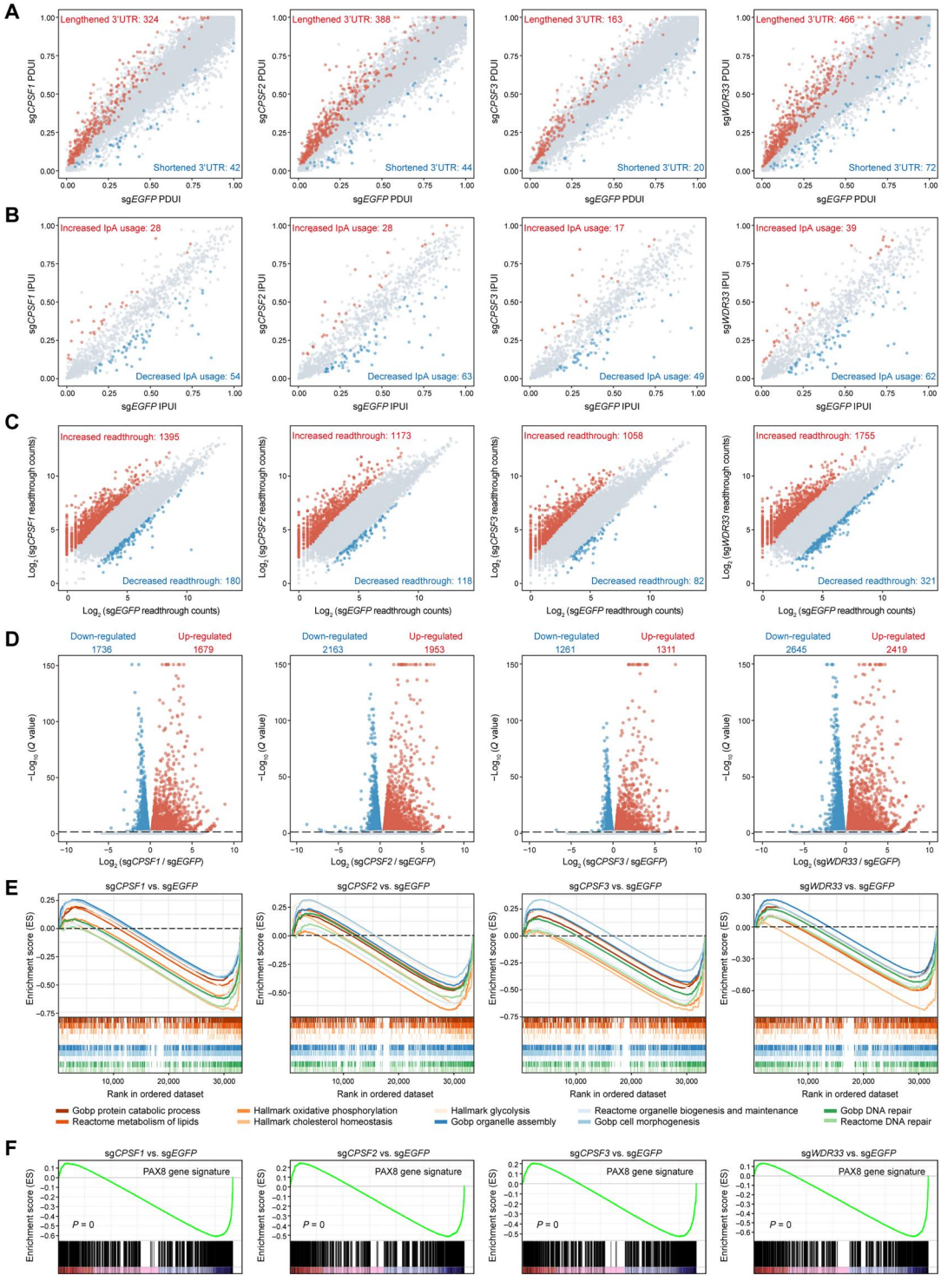

Fig. 3. Altered pre-mRNA 3′-end processing and gene expression upon CPSF depletion. (**A**) Scatter plots of percentage of distal poly(A) site usage index (PDUI) values reflecting the relative distal-to-proximal PAS usage in SKOV3 cells with *CPSF1*, *CPSF2*, *CPSF3*, or *WDR33* knockout. Transcripts with lengthened or shortened 3′UTR upon gene knockout in comparison to control cells are shown in red or blue, respectively. (**B**) Scatter plots of IPUI intronic poly(A) site usage index (IPUI) values reflecting the relative IpA usage in SKOV3 cells with *CPSF1*, *CPSF2*, *CPSF3*, or *WDR33* knockout. Transcripts with increased or decreased IpA usage upon gene knockout in comparison to control cells are shown in red or blue, respectively. (**C**) Scatter plots of readthrough counts in SKOV3 cells with *CPSF1*, *CPSF2*, *CPSF3*, or *WDR33* knockout. Transcripts with significantly increased or decreased readthrough counts upon gene knockout in comparison to control cells are shown in red or blue, respectively. (**D**) Volcano plots showing differentially expressed genes in SKOV3 cells with *CPSF1*, *CPSF2*, *CPSF3*, or *WDR33* knockout. Transcripts with significant up-regulation or down-regulation upon gene knockout in comparison to control cells are shown in red or blue, respectively. (**E**) GSEA plots showing disproportionate down-regulation of genes involved in cell metabolism, organelle biogenesis, and DNA repair in SKOV3 cells with *CPSF1*, *CPSF2*, *CPSF3*, or *WDR33* knockout. (**F**) GSEA plots showing disproportionate down-regulation of PAX8 gene signature in SKOV3 cells with *CPSF1*, *CPSF2*, *CPSF3*, or *WDR33* knockout.

ring for cross-linking target proteins upon ultraviolet irradiation and an alkyne handle for click chemistry–mediated cycloaddition of biotin-azide. Incubation with XHJ1167, but not HQY54, enabled affinity capture of conjugated CPSF3 from SKOV3 cell lysate, which was completely abrogated by pretreatment of HQY426 or HQY436, but not HQY429 (Fig. 5D). Fluorescence polarization assays indicated that the binding affinity of HQY426, HQY436, and XHJ1049 to purified CPSF3 protein, with an estimated median inhibitory concentration of 0.32, 0.15, and 0.24 μM, respectively, was appreciably higher than that of HQY429 (~6 μM) and JTE-607 (>10 μM) (Fig. 5E).

To determine the specificity of CPSF3 inhibitors, we substituted a predicted key residue alanine-395 on CPSF3 by threonine (A395T) to impair drug interaction (fig. S9C) (*55*). Overexpression

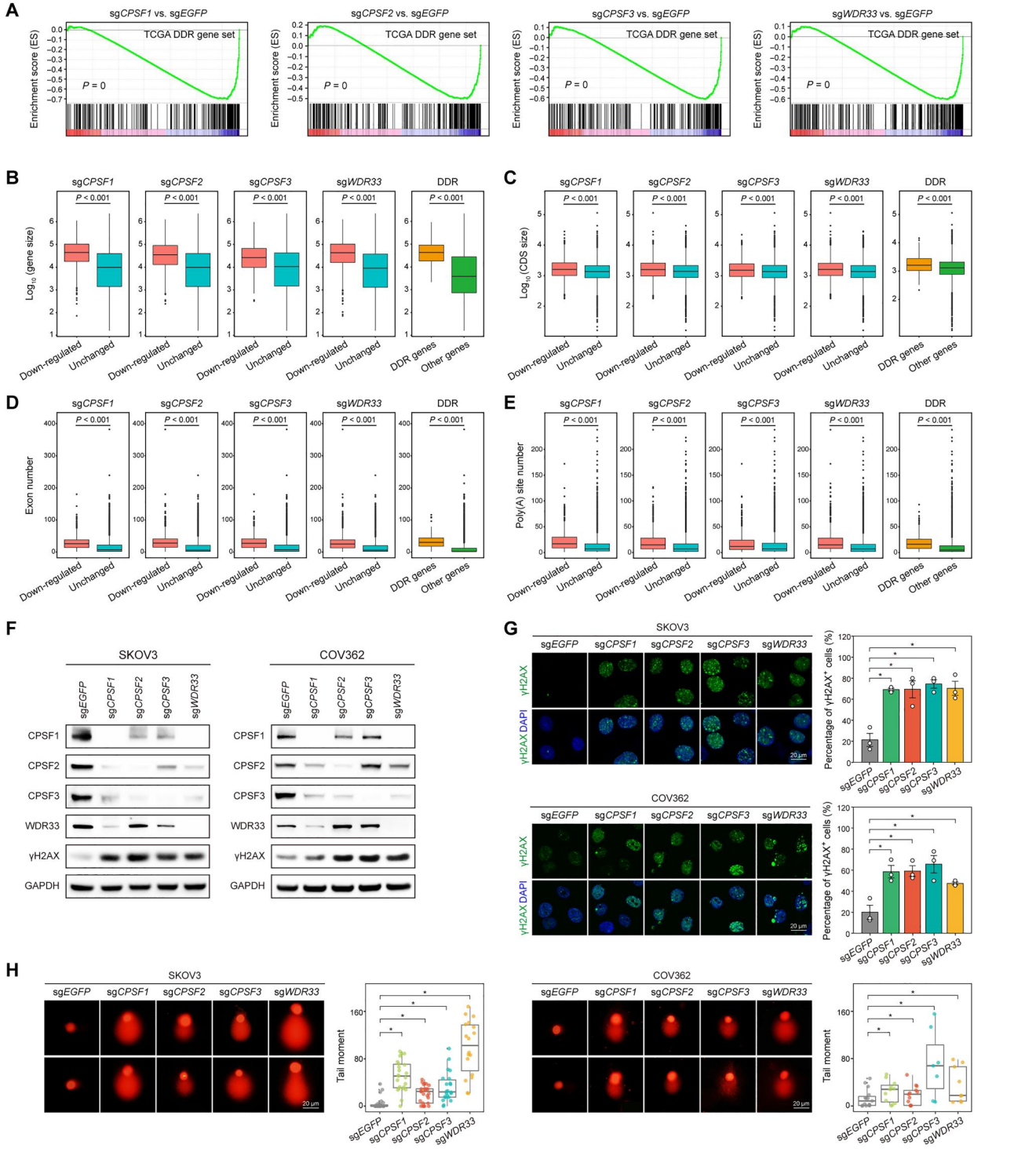

Fig. 4. Attenuated DDR upon CPSF depletion. (**A**) GSEA plots showing disproportional down-regulation of a 276-member gene set related to DDR defined by TCGA in SKOV3 cells with *CPSF1*, *CPSF2*, *CPSF3*, or *WDR33* knockout. (**B** to **E**) Boxplots showing comparison of gene sizes, coding sequence (CDS) sizes, exon numbers, and PAS numbers between significantly down-regulated and nondifferentially expressed genes in SKOV3 cells with *CPSF1*, *CPSF2*, *CPSF3*, or *WDR33* knockout. The gene sizes, coding sequence sizes, exon numbers, and PAS numbers were also compared between 276 DDR genes defined by TCGA and other genes. The difference between each two groups is statistically significant ($P < 0.001$, two-tailed Wilcoxon test). (**F**) Immunoblotting analysis of the indicated proteins in SKOV3 and COV362 cells with *CPSF1*, *CPSF2*, *CPSF3*, or *WDR33* knockout. Glyceraldehyde-3-phosphate dehydrogenase was used as the loading control. (**G**) Immunofluorescence staining of γH2AX (green) in SKOV3 and COV362 cells with *CPSF1*, *CPSF2*, *CPSF3*, or *WDR33* knockout. Cell nuclei were counterstained with DAPI (blue). Quantification on the percentage of cells containing more than five γH2AX foci is plotted as means ± SD ($n = 3$). *$P < 0.05$, ANOVA followed by Tukey's posttest. Scale bars, 20 μm. (**H**) Representative images and quantitative analysis of comet assay in SKOV3 and COV362 cells with *CPSF1*, *CPSF2*, *CPSF3*, or *WDR33* knockout. Tail moment = tail DNA % × tail moment length. *$P < 0.05$, ANOVA followed by Tukey's posttest. Scale bars, 20 μm.

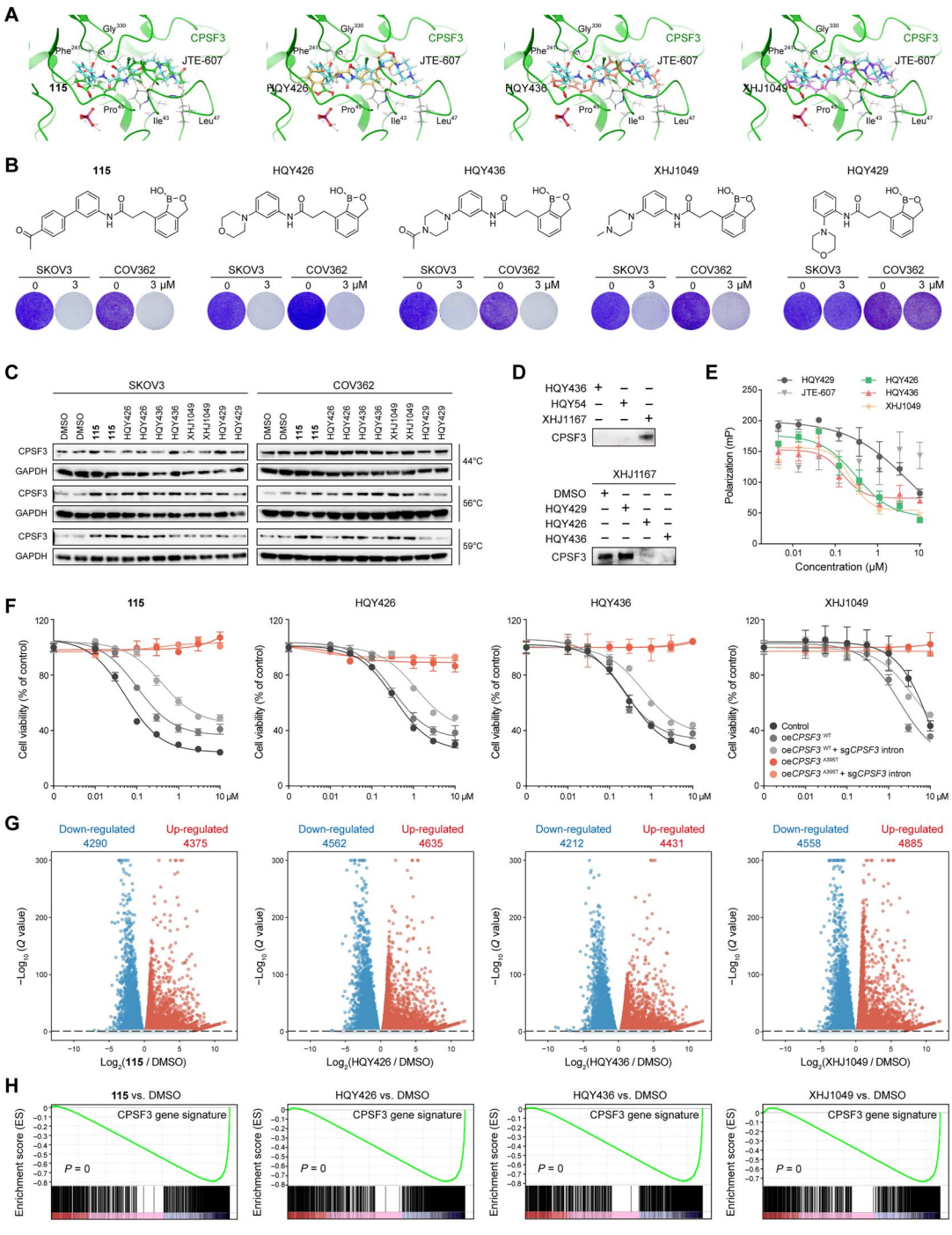

Fig. 5. Discovery of benzoxaborole-based CPSF3 inhibitors. (**A**) Molecular docking analysis of **115** (green), HQY426 (yellow), HQY436 (orange), or XHJ1049 (purple) against the active site of CPSF3 (Protein Data Bank ID: 6M8Q). In the predicted binding mode, **115**, HQY426, HQY436, or XHJ1049 adopted a conformation very close to that of JTE-607 (blue) in complex with CPSF3 from their cocrystal structure. (**B**) Chemical structures of **115**, HQY426, HQY436, XHJ1049, and HQY429. Cell viability was assayed by crystal violet staining in SKOV3 and COV362 cells treated with indicated compounds. (**C**) SKOV3 and COV362 cells were treated with dimethyl sulfoxide (DMSO), **115**, HQY426, HQY436, XHJ1049, or HQY429 and subjected to cellular thermal shift assay. CPSF3 was analyzed by immunoblotting. (**D**) SKOV3 cells were treated with HQY436, HQY54, or XHJ1167 (0.3 μM), followed by ultraviolet irradiation and click chemistry conjugation with biotin-azide. Proteins captured with streptavidin beads were analyzed by immunoblotting. Competitive photocrosslinking assay was performed by pretreating SKOV3 cells with excessive unlabeled compounds (10 μM) before XHJ1167 (0.3 μM) was added. (**E**) CPSF3 protein was purified and incubated with indicated compounds. A fluorescent probe was added, and the fluorescence polarization was recorded. Dose-response curves were constructed to determine the median inhibitory concentration values as measures of binding affinity. (**F**) Wild-type or mutant *CPSF3* was overexpressed in SKOV3 cells with or without endogenous *CPSF3* knockout. Cells were treated with various concentrations of **115**, HQY426, HQY436, or XHJ1049 for 72 hours, and cell viability was measured by the Cell Count Kit-8 (CCK-8) assay. (**G**) Volcano plots showing differentially expressed genes in SKOV3 cells treated with **115**, HQY426, HQY436, or XHJ1049 for 6 hours. (**H**) GSEA plots showing disproportionate down-regulation of CPSF3 gene signature in SKOV3 cells treated with **115**, HQY426, HQY436, or XHJ1049 for 6 hours.

of this CPSF3 mutant almost fully rescued the antineoplastic effects exerted by CPSF3 blockade, as demonstrated by dose-response curves (Fig. 5F) and crystal violet staining (fig. S9D). Although other possible targets could not be ruled out, we surmised that CPSF3 served as the primary functional substrate of these 7-propanamide benzoxaboroles in ovarian cancer. Furthermore, RNA-seq profiling on SKOV3 cells treated with CPSF3 antagonists recapitulated major transcriptomic changes caused by *CPSF3* knockout. Specifically, there were 357 to 408 genes with lengthened 3′UTR in comparison to 160 to 341 genes with shortened 3′UTR (fig. S10A and tables S18 to S21). In addition, IpA usage tended to be decreased (fig. S10B and tables S22 to S25). We identified 4143 to 4471 readthrough transcripts beyond the annotated 3′UTR boundary (fig. S10C and tables S26 to S29), including

PAX8 and *ARHGAP29* (fig. S10D). Notably, differentially expressed genes induced by the four compounds were largely shared (Fig. 5G and tables S30 to S33) and enriched for CPSF3 gene signature (Fig. 5H), reinforcing CPSF3 as the major drug target. Again, correlation matrix heatmaps highlighted that global events of APA (fig. S10E), IpA (fig. S10F), transcriptional readthrough (fig. S10G), and differential gene expression (fig. S10H) were each significantly correlated in SKOV3 cells exposed to **115**, HQY426, HQY436, and XHJ1049. Together, we found a collection of benzoxaborole-based CPSF3 inhibitors.

Potent antitumor efficacy of CPSF3 inhibitors

To establish the translational relevance of targeted CPSF3 therapy, we used a larger panel of ovarian cancer cell lines to validate the antineoplastic effects of newly designed CPSF3 inhibitors. HQY426 and HQY436, two lead candidates with higher potency, showed consistent evidence of antitumor efficacy, as demonstrated by dose-response curves (Fig. 6A) and crystal violet staining (fig. S11A). At the cellular level, HQY426 or HQY436 exposure, in keeping with *CPSF3* depletion, suppressed cell proliferation (Fig. 6B) and caused G_2-M arrest (Fig. 6C). Moreover, HQY426 and HQY436 triggered robust cell apoptosis, as assessed by immunoblotting analysis of cleaved PARP and caspase 3/7 (Fig. 6D). To evaluate the in vivo activity of CPSF3 inhibitors, we first probed the pharmacokinetic properties of HQY426 and HQY436 in mice following oral, intraperitoneal, and intravenous injection (fig. S11B). Dose-normalized oral bioavailability (F) of HQY426 and HQY436 was 47.24 and 13.86%, respectively (fig. S11C), which was greatly improved as compared to 4.6% reported for **115**. Notably, intraperitoneal dosing yielded relatively higher absolute bioavailability than that via oral gavage compared with intravenous administration as the reference standard. Thus, we intraperitoneally inoculated SKOV3 cells and dosed the BALB/c nude mice at 10 mg/kg per day. HQY426 treatment of SKOV3 xenotransplants resulted in markedly reduced abdominal masses (Fig. 6E). There was a twofold decrease in overall tumor burden (Fig. 6F) without significant loss of body weight (Fig. 6G); histological abnormality in the heart, liver, spleen, lung, and kidney (fig. S12A); or hematological and biochemical changes in plasma (fig. S12B). In line with the in vitro data, we observed impaired cell proliferation as indicated by Ki67 staining and increased cell apoptosis as detected by caspase 3/7 cleavage (Fig. 6H). Therefore, CPSF3 inhibitors exhibited potent therapeutic efficacy and low systemic toxicity, supporting further development in ovarian cancer.

Synergistic effects of CPSF3 and PARP inhibition in ovarian cancer

Consistent with the antitumor activity of CPSF3 inhibitors and prior findings in CPSF-ablated SKOV3 cells, Cytoscape analysis of RNA-seq data pinpointed that pharmacological CPSF3 inhibition using HQY426 or HQY436 disrupted RNA metabolism, cell cycle process, and, most intriguingly, DNA damage response (fig. S13A). GSEA plots confirmed disproportional down-regulation of the 276-member DDR gene set defined by TCGA (Fig. 7A). When grouped into major DNA repair pathways (fig. S13B), DDR genes involved in homology-dependent recombination (HDR) were more profoundly affected by HQY426 or HQY436 treatment (Fig. 7B), implying that a BRCAness phenotype could be provoked. These observations were corroborated by quantitative polymerase chain reaction analysis on in vivo samples showing altered pre-mRNA 3′-end processing or gene expression of cancer-related (fig. S13C), DDR (fig. S13D), and HDR (fig. S13E) genes upon CPSF3 blockade. Accordingly, an evident increase in γH2AX foci and protein abundance in drug-exposed SKOV3 cells was detected by immunofluorescence staining (Fig. 7C) and Western blot (Fig. 7D), respectively. Similar results were also observed in COV362 cells (fig. S14A). Moreover, comet assay illustrated elevated tail moment (Fig. 7E), suggesting the accumulation of DNA strand breaks. Thus, we hypothesized that a synthetic lethal interaction might exist between CPSF3 and PARP inhibitors against ovarian cancer. Combination therapy of HQY426 or HQY436 with olaparib induced higher levels of γH2AX aggregates than either agent alone in SKOV3 cells (Fig. 7F). Consequently, dose matrix experiments established marked synergy between HQY426 or HQY436 and olaparib in SKOV3 (Fig. 7G), COV362 (fig. S14B), PA-1 (fig. S14C), and ES-2 cells (fig. S14D). In agreement with the findings in cell culture, when SKOV3 xenografts were cotreated with HQY426 (10 mg/kg per day) and olaparib (50 mg/kg per day), HQY426 synergized with olaparib to inhibit tumor growth in mice (Fig. 7H). Consistently, combined treatment was associated with further enhanced DNA damage as shown by γH2AX immunohistochemistry, more markedly impaired cell proliferation as indicated by Ki67 staining, and a larger increase of cell apoptosis as detected by caspase 3/7 cleavage (fig. S15A). Meantime, no significant loss of body weight (Fig. 7I) or histological abnormality in the heart, liver, spleen, lung, and kidney (fig. S15B) was noted. On the basis of these data, we concluded that targeting CPSF3-dependent transcriptional termination caused functional deficiencies in DDR and rendered ovarian cancer susceptible to PARP inhibitors.

DISCUSSION

In this study, we systematically interrogated the oncogenic function of central players governing transcriptional termination and explicitly implicated the CPSF complex in promoting ovarian cancer growth. Applying various algorithms to CPSF-associated transcriptomic landscape revealed that its protumorigenic nature was attributable to the pervasive regulation of pre-mRNA 3′-end processing and neoplastic gene expression. The endonucleolytic subunit CPSF3 was identified as a pivotal and druggable target, which was exemplified by our discovery of benzoxaborole-derived CPSF3 inhibitors and the profound preclinical efficacy against ovarian cancer. CPSF3 antagonists induced robust DNA damage, resulting in synthetic lethality in conjunction with PARP inhibition. Collectively, these investigations (summarized in fig. S16) demonstrated the feasibility and effectiveness of targeting CPSF3-dependent transcriptional termination as a promising therapeutic avenue for the treatment of ovarian cancer and potentially other human malignancies driven by aberrant transcription.

The present work has added to the growing body of evidence indicating exquisite transcriptional addiction embedded in ovarian cancer pathobiology. Although transcriptional dysregulation is a notorious hallmark of cancer, most exploration has historically focused on initiation and elongation (*8*, *57*, *58*). There is a plethora of elegant examples in literature illustrating the indispensability of core machinery underpinning the early phases of transcription cycle. Meanwhile, APA has been increasingly recognized as a widespread phenomenon during cancer onset and progression, causing

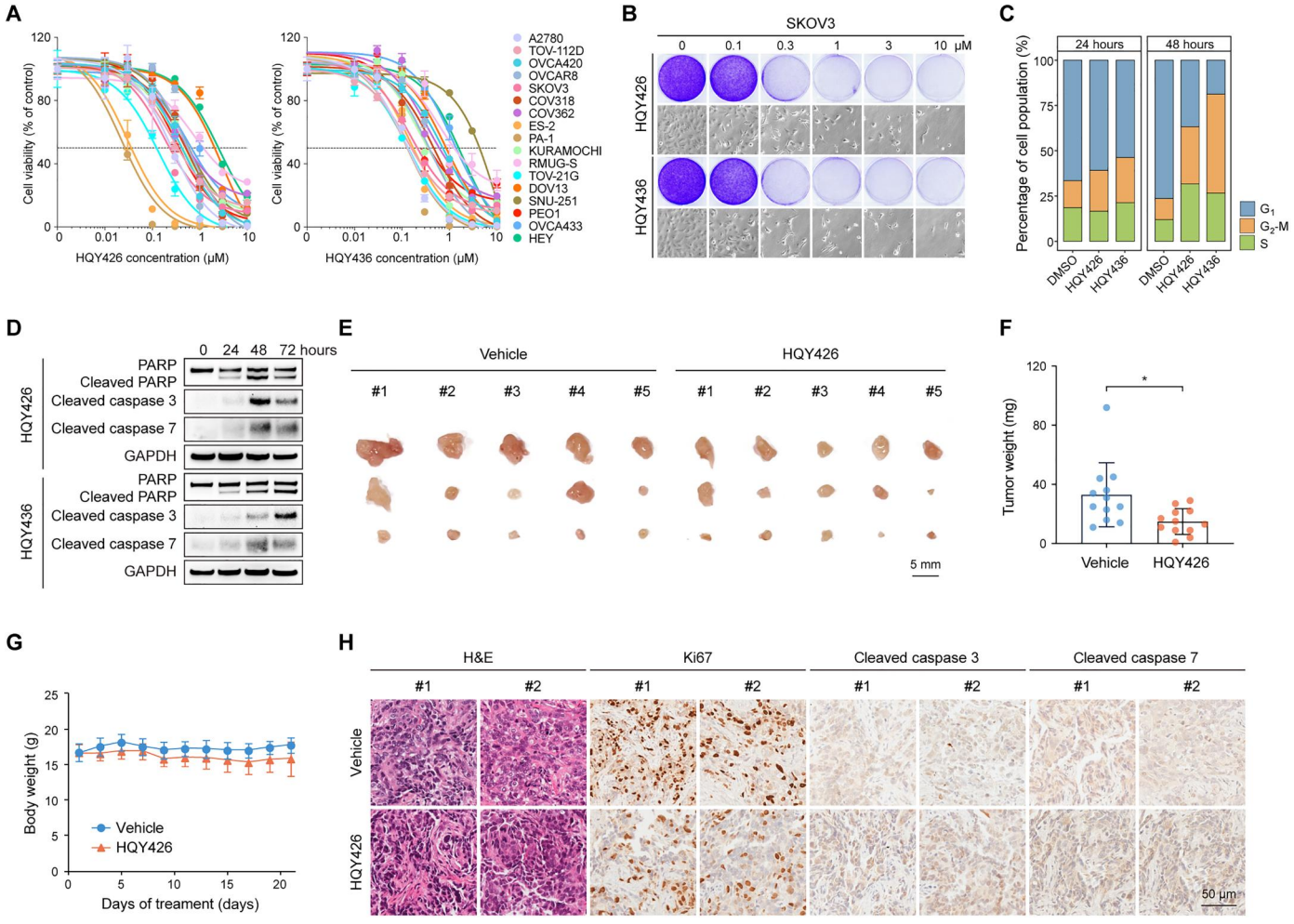

Fig. 6. Potent antitumor efficacy of CPSF3 inhibitors. (**A**) Cell viability was measured by the CCK-8 assay in a panel of ovarian cancer cell lines treated with various concentrations of HQY426 or HQY436 for 72 hours. (**B**) SKOV3 cells were treated with HQY426 or HQY436 at various concentrations, and cell viability was determined by crystal violet staining and phase-contrast microscopy. (**C**) Cell cycle analysis by flow cytometry on SKOV3 cells treated with HQY426 or HQY436 for 24 and 48 hours. Values are expressed as percentage of the cell population in the G_1, S, or G_2-M phase of cell cycle. (**D**) Cell apoptosis induced by HQY426 or HQY436 treatment in a time course was documented by immunoblotting analysis of cleaved PARP and cleaved caspase 3/7. (**E**) Representative images of SKOV3 xenografts from BALB/c nude mice treated with HQY426 (10 mg/kg per day) or vehicle control [5% ethanol (EtOH), 5% DMSO, and 40% polyethylene glycol, poly(ethylene glycol) 400 (PEG-400)] for 21 days. The three largest tumors shown for each mouse were dissected from distinct abdominal sites. Scale bar, 5 mm. (**F**) Quantification of SKOV3 tumor weight in the vehicle control and HQY426-treated groups. The tumor weight for each mouse was calculated by adding the weights of all resectable implants. *$P < 0.05$, unpaired Student's t test. (**G**) Body weight measurements of BALB/c nude mice during HQY426 (10 mg/kg per day) or vehicle (5% EtOH, 5% DMSO, and 40% PEG-400) treatment. (**H**) Representative images of hematoxylin and eosin (H&E) and immunohistochemistry staining for Ki67, cleaved caspase 3, or cleaved caspase 7 in SKOV3 tumor slices. Scale bar, 50 μm.

broad 3′UTR shortening, which fine-tunes gene expression and correlates with enhanced aggressive behavior (*59*–*61*). Previously, multiple functional modules of the transcriptional termination apparatus, including CstF, CFIm, and CFIIm, have been each proven to facilitate carcinogenesis by modulating APA (*62*–*64*). Our findings complement existing research by uncovering the prominent role of CPSF complex in ovarian cancer. It is worth mentioning that PCF11 cleavage and polyadenylation factor subunit (PCF11) and cleavage factor polyribonucleotide kinase subunit 1 (CLP1) in the CFIIm complex seemed to be required for ovarian cancer as well, and future research is warranted to thoroughly elucidate its function. In contrast, most other tested factors appeared to be largely dispensable. The differential reliance on distinct regulatory elements in diverse tumor types points to an appealing model of tissue-specific context-dependent essentiality, which remains to be further assessed. Moreover, despite the seemingly universal involvement of termination programs in both physiological and pathological conditions, malignant cells often feature genetic and epigenetic alterations ultimately converging on deviated transcriptional control, which may offer relative selectivity and potential opportunities for therapeutic interventions.

The CPSF complex couples PAS recognition in the nascent pre-mRNA with cleavage and polyadenylation. Despite extensive literature on its conserved competence to carry out canonical 3′-end processing, less is known about the biological significance of individual subunits in human neoplasms. Recent in vitro reconstitution and structural analyses have illuminated mechanistic insights into the protein composition and modular organization of CPSF complex.

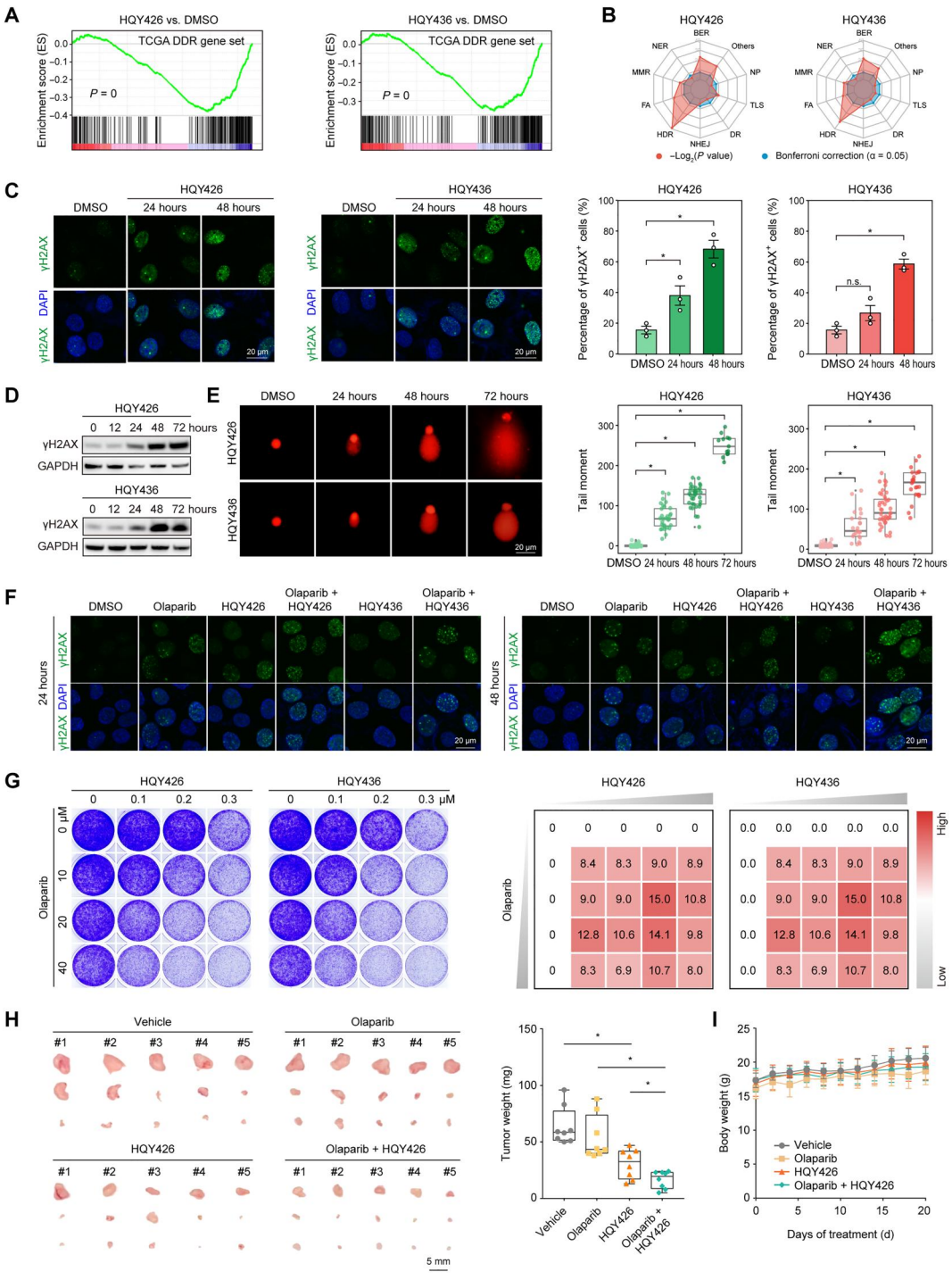

Fig. 7. Synergistic effects of CPSF3 and PARP inhibition in ovarian cancer. (**A**) GSEA plots showing disproportional down-regulation of a 276-member gene set related to DDR defined by TCGA in SKOV3 cells treated with HQY426 or HQY436. (**B**) Radar plots showing relative enrichment of different DDR pathways in SKOV3 cells treated with HQY426 or HQY436. (**C**) Immunofluorescence staining of γH2AX (green) in SKOV3 cells treated with HQY426 or HQY436 for 24 or 48 hours. Quantification on the percentage of cells containing more than five γH2AX foci is plotted as means ± SD (n = 3). *P < 0.05, ANOVA followed by Tukey's posttest. Scale bars, 20 μm. (**D**) Immunoblotting analysis of γH2AX in SKOV3 cells treated with HQY426 or HQY436 in a time course manner. (**E**) Representative images and quantitative analysis of comet assay in SKOV3 cells treated with HQY426 or HQY436 for indicated time. Tail moment = tail DNA % × tail moment length. *P < 0.05, ANOVA followed by Tukey's posttest. Scale bar, 20 μm. (**F**) Immunofluorescence staining of γH2AX (green) in SKOV3 cells treated with indicated inhibitors for 24 or 48 hours. Scale bars, 20 μm. (**G**) Crystal violet staining of dose response assays and heatmaps of bliss synergy scores demonstrated synergistic activities of HQY426 or HQY436 and olaparib in SKOV3 cells. (**H**) Representative images of SKOV3 xenografts from BALB/c nude mice treated with vehicle control, HQY426 (10 mg/kg per day) or olaparib (50 mg/kg per day), and quantification of SKOV3 tumor weight in indicated groups. Scale bar, 5 mm. The tumor weight for each mouse was calculated by adding the weights of all resectable implants. *P < 0.05, ANOVA followed by Tukey's posttest. (**I**) Body weight measurements of BALB/c nude mice during indicated treatment.

In detail, the mPSF subcomplex contains CPSF1, WDR33, CPSF4, and FIP1L1 and is responsible for PAS binding and poly(A) polymerase recruitment (*65*, *66*). On the other hand, the mCF subcomplex, mainly consisting of CPSF2 and CPSF3, interacts with the heterodimeric CPSF1-WDR33 scaffold and cleaves nascent RNA species (*39*). Our observation of dichotomous outcomes following experimental manipulation of the two subcomplexes underscored the exclusive requirement of mCF function in ovarian cancer, implying that the occurrence rather than the fidelity of cleavage event imparts more influence on transcriptional output. Corroborating this hypothesis, loss of any identified vital subunits in CPSF complex invariably down-regulated the dedicated endonuclease CPSF3, yielding a plausible explanation for the convergence in both phenotypic and transcriptomic findings with genetic knockout. Additional efforts are desired to address whether accelerated protein turnover succeeding CPSF complex perturbation contributes to the CPSF3 reduction. Regardless of the underlying mechanism, exogenous CPSF3 failed to compensate the deficits, in

concordance with the fact that CPSF3 has weak enzymatic activity in isolation and needs concerted action with other constituents for efficient transcript cleavage (*40*). It is also tempting to speculate that the CPSF complex is encapsulated through phase separation, as with other high-order multiprotein assemblies of transcriptional regulators (*67*–*70*). In support of such a possibility, nearly all CPSF subunits are predicted to harbor intrinsically disordered regions.

Considering the current paucity of rational therapeutics in ovarian cancer, we describe a drug discovery campaign to pharmacologically block the CPSF complex. CPSF3, a zinc-dependent hydrolase of the metallo-β-lactamase family, serves as the key catalytic component that is presumably amenable to small-molecule inhibition (*28*, *29*). Consistent with this notion, prior work has unveiled JTE-607 as a prodrug against CPSF3 that inhibits acute myeloid leukemia and Ewing′s sarcoma (*55*). However, such a negative impact was not observed in ovarian cancer cells, indicating the lineage-restricted sensitivity to JTE-607. In addition, benzoxaboroles are boron-heterocyclic molecules known to specifically engage microbial or protozoal CPSF3 with the oxaborole moiety coordinated to the zinc ions but display minimal cross-reactivity with its human counterpart (*51*–*54*). **115**, representing 7-propanamide benzoxaboroles, has been found to exert potent antitumor effects without defined mode of action (*56*). We postulated that CPSF3 could be the bona fide target of this unique compound family. **115** and our optimized derivatives, e.g., HQY426, were demonstrated to interact and interfere with CPSF3 based on a string of biochemical and bioinformatics analysis. In cell-based assays, HQY426 exhibited marked antiproliferative and proapoptotic capacity. In animal studies, HQY426 was well tolerated and significantly impeded xenograft growth in vivo. Overall, these data highlight a viable pharmacological approach of CPSF3 modulation. Although several benzoxaboroles have been approved for human use, the safety of 7-propanamide benzoxaboroles requires more rigorous evaluation. In addition, future structural characterization of CPSF3 protein in complex with HQY426, together with lately reported real-time fluorescence assay for probing CPSF3 nuclease activity (*71*), may shed light on next-generation innovative inhibitors with ameliorated antineoplastic efficacy and favorable physicochemical properties for clinical development.

Our results argue that transcriptional interruption of critical oncogenic pathways, instead of deleterious RNA structure formation, predominantly accounts for tumor cell suppression upon CPSF complex disturbance. In agreement with this view, genetic or pharmacological CPSF3 inhibition caused lengthened 3′UTRs, repressed IpA, and, more notably, extended transcriptional readthrough, cumulatively leading to a multitude of differentially expressed genes. CPSF3 perturbation did not indiscriminately alter global transcription but rather more selectively impeded gene expression of DDR enzymes. Consequently, a BRCAness phenotype was induced, producing a compelling rationale to combine CPSF3 and PARP inhibitors. Notably, analogous BRCAness state arises from CDK12 blockade or its loss-of-function mutations, which aggravate IpA to generate truncated mRNA isoforms (*72*–*74*). At first glance, it seems counterintuitive that both precocious and delayed termination preferentially affect the same set of transcripts. While the exact molecular mechanisms remain to be elucidated, it is likely that DDR genes are generally long with extra polyadenylation sites and are thus prone to abnormal pre-mRNA 3′-end processing. Therefore, a common theme that emerges is the multifaceted interplay between transcriptional homeostasis and genomic integrity. We propose that concomitant targeting of transcriptional termination will broaden the utility of PARP inhibitors by harnessing synthetic lethality.

In conclusion, we pinpoint CPSF3-dependent transcriptional termination as an actionable vulnerability in ovarian cancer and present proof-of-concept therapeutic regimens by developing and evaluating a class of CPSF3 inhibitors. A deeper understanding of transcriptionally addicted tumors and continued discovery of transcription-targeted compounds hold enormous promise to improve patient treatment and survival in the oncology setting.

MATERIALS AND METHODS

Cell lines and reagents

Ovarian cancer cell lines and human embryonic kidney (HEK) 293T were purchased from the American Type Culture Collection or Japanese Collection of Research Bioresources Cell Bank. All cell lines were routinely tested for mycoplasma contamination and cell identity by short tandem repeat profiling. Cells were maintained in RPMI 1640 (Life Technologies) supplemented with 10% fetal bovine serum (Gibco), D-glutamine (2 mM), penicillin (100 U/ml), and streptomycin (100 μg/ml). Commercial small-molecule inhibitors were purchased from Selleck Chemicals and reconstituted in dimethyl sulfoxide (DMSO; Sigma-Aldrich) at a stock concentration of 10 mM.

Cell viability assays and combination matrices

Cell viability was estimated by crystal violet staining or Cell Count Kit-8 (CCK-8) assay (ShareBio). For crystal violet staining, cells were seeded at 50,000 cells per well in six-well plates, allowed to adhere overnight, and treated with a serial dilution of inhibitors for 5 days. Cells were fixed with formalin and stained with crystal violet. For CCK-8 assay, cells were seeded in triplicate in 96-well plates at 3000 to 5000 cells per well and subjected to indicated treatments for 72 hours before measuring the absorbance at 450 nm. To measure drug combination effects, the Bliss synergy scores were calculated by the equation $(A + B) - A \times B$. A or B was the fractional growth inhibition induced by agent A or B at a given dose.

Immunofluorescence staining

Cells grown on an eight-well culture dish (Ibidi) were fixed with 4% paraformaldehyde for 15 min at room temperature (RT) and permeabilized with 0.1% Triton X-100 (Sigma-Aldrich) in phosphate-buffered saline (PBS) for 10 min. After washing three times in PBS, cells were blocked with 2% bovine serum albumin in PBS for 30 min at RT before incubation with primary antibodies against γH2AX (#80312, Cell Signaling Technology) and R-loop (ENH001, Kerafast) at 4°C overnight. After three washes in PBS, cells were incubated with fluorescent secondary antibodies Alexa Fluor 488–labeled anti-mouse immunoglobulin G (A11029, Invitrogen) at RT for 1 hour in the dark. Cells were washed with PBS, followed by 4′,6-diamidino-2-phenylindole (DAPI; Invitrogen) counterstaining for 5 min. Images were observed using confocal laser scanning microscopy (Leica).

Comet assay

Cells were genetically edited or treated with indicated compounds before neutral comet assays were performed. A total of 8000 cells in

0.4 ml of PBS were added to 1.2 ml of 1% low gelling temperature agarose (Trevigen) and pipetted onto comet slides (Trevigen). Once the gel solidified, slides were incubated in prechilled neutral lysis buffer [2% sarkosyl, 0.5 M Na_2-EDTA, and proteinase K (0.5 mg/ml) (pH 8.0)] at 37°C overnight in the dark. On the following day, the slides were submerged in neutral rinse buffer [90 mM boric acid, 2 mM Na_2-EDTA, and 90 mM tris-HCl (pH 8.5)] for 20 min at RT and then electrophoresed at 20 V/cm for 40 min at 4°C. After washes, slides were stained with SYBR Gold (Life Technologies) in PBS at RT for 30 min in the dark and observed under a fluorescence microscope (Leica). Cells in each sample were evaluated and quantified by the Comet Assay software project (version 1.2.3b1) to determine the tail length and tail moment.

In vivo studies

To evaluate the function of CPSF complex in vivo, luciferase-labeled SKOV3 cells (1×10^6) with *CPSF1*, *CPSF2*, *CPSF3*, *WDR33*, *CPSF4*, or *FIP1L1* genetic depletion were intraperitoneally injected into the female BALB/c nude mice (5 weeks of age). Tumor growth was monitored by bioluminescence imaging once a week. For imaging, mice were injected with 1.5 mg of D-luciferin (15 mg/ml in PBS) and then anesthetized with isoflurane. Images were acquired within 8 min after injection with an IVIS Spectrum CT instrument coupled to Living Image acquisition software (PerkinElmer). Images were analyzed with Living Image software (version 4.5). Bioluminescent flux (in photons per second per square centimeter per steradian) was determined for all mice in a prone position. For single-agent treatment of tumor-bearing mice, SKOV3 cells (1×10^6) were intraperitoneally injected into the female BALB/c nude mice (5 weeks of age). The CPSF3 inhibitor HQY426 was administered by intraperitoneal injection at a dose of 10 mg/kg per day, using vehicle [5% (v/v) DMSO, 5% (v/v) ethanol (EtOH), and 40% (v/v) polyethylene glycol, molecular weight 400 (PEG-400)] as the negative control. For combination treatment, HQY426 was given at a dose of 10 mg/kg per day by intraperitoneal injection, and olaparib was given at a dose of 50 mg/kg per day through oral medication. Mice were monitored and weighed every other day. After 3 weeks, mice were euthanized, and tumor tissues were harvested and fixed in 4% paraformaldehyde for immunohistochemistry of Ki67 (#9027, Cell Signaling Technology), γH2AX (#80312, Cell Signaling Technology), cleaved caspase 3 (#9661, Cell Signaling Technology), and cleaved caspase 7 (#8438, Cell Signaling Technology). The institutional animal care and use committee of Ren Ji Hospital approved animal protocols, and all experiments were performed in accordance with Ren Ji Hospital policies on the care, welfare, and treatment of laboratory animals.

Statistical analysis

The sequencing data were deposited in the National Center for Biotechnology Information (NCBI) BioProject database under the accession number PRJNA892709. For DepMap datasets, dependency scores for each gene of interest in ovarian cancer cell lines were downloaded from the DepMap web portal (https://depmap.org/portal). GSEA was performed using the GSEA software (v4.1.0). Gene ontology and pathway analyses were performed using Metascape, and network visualizations were generated with Cytoscape. Pearson's correlation coefficient was used to measure the linear correlation between two variables. In all experiments, comparisons between two groups were based on a two-sided Student's *t* test. All graphics and statistics were generated using GraphPad Prism (v8.0) or R (v4.1.0). *P* values of <0.05 were considered statistically significant.

Supplementary Materials

This PDF file includes:
Supplementary Methods
Figs. S1 to S16
Legend for data S1
References

Other Supplementary Material for this manuscript includes the following:
Data S1

REFERENCES AND NOTES

1. S. Lheureux, C. Gourley, I. Vergote, A. M. Oza, Epithelial ovarian cancer. *Lancet* **393**, 1240–1253 (2019).
2. R. L. Siegel, K. D. Miller, H. E. Fuchs, A. Jemal, Cancer statistics, 2022. *CA Cancer J. Clin.* **72**, 7–33 (2022).
3. L. Kuroki, S. R. Guntupalli, Treatment of epithelial ovarian cancer. *BMJ* **371**, m3773 (2020).
4. E. Franzese, S. Centonze, A. Diana, F. Carlino, L. P. Guerrera, M. di Napoli, F. de Vita, S. Pignata, F. Ciardiello, M. Orditura, PARP inhibitors in ovarian cancer. *Cancer Treat. Rev.* **73**, 1–9 (2019).
5. K. Odunsi, Immunotherapy in ovarian cancer. *Ann. Oncol.* **28**, viii1–viii7 (2017).
6. U. A. Matulonis, R. Shapira-Frommer, A. D. Santin, A. S. Lisyanskaya, S. Pignata, I. Vergote, F. Raspagliesi, G. S. Sonke, M. Birrer, D. M. Provencher, J. Sehouli, N. Colombo, A. González-Martín, A. Oaknin, P. B. Ottevanger, V. Rudaitis, K. Katchar, H. Wu, S. Keefe, J. Ruman, J. A. Ledermann, Antitumor activity and safety of pembrolizumab in patients with advanced recurrent ovarian cancer: Results from the phase II KEYNOTE-100 study. *Ann. Oncol.* **30**, 1080–1087 (2019).
7. The Cancer Genome Atlas Research Network, Integrated genomic analyses of ovarian carcinoma. *Nature* **474**, 609–615 (2011).
8. J. E. Bradner, D. Hnisz, R. A. Young, Transcriptional addiction in cancer. *Cell* **168**, 629–643 (2017).
9. G. L. Hager, J. G. McNally, T. Misteli, Transcription dynamics. *Mol. Cell* **35**, 741–753 (2009).
10. J. Shandilya, S. G. Roberts, The transcription cycle in eukaryotes: From productive initiation to RNA polymerase II recycling. *Biochim. Biophys. Acta* **1819**, 391–400 (2012).
11. M. J. Bywater, R. B. Pearson, G. A. McArthur, R. D. Hannan, Dysregulation of the basal RNA polymerase transcription apparatus in cancer. *Nat. Rev. Cancer* **13**, 299–314 (2013).
12. M. Heidemann, C. Hintermair, K. Voß, D. Eick, Dynamic phosphorylation patterns of RNA polymerase II CTD during transcription. *Biochim. Biophys. Acta* **1829**, 55–62 (2013).
13. N. Kwiatkowski, T. Zhang, P. B. Rahl, B. J. Abraham, J. Reddy, S. B. Ficarro, A. Dastur, A. Amzallag, S. Ramaswamy, B. Tesar, C. E. Jenkins, N. M. Hannett, D. McMillin, T. Sanda, T. Sim, N. D. Kim, T. Look, C. S. Mitsiades, A. P. Weng, J. R. Brown, C. H. Benes, J. A. Marto, R. A. Young, N. S. Gray, Targeting transcription regulation in cancer with a covalent CDK7 inhibitor. *Nature* **511**, 616–620 (2014).
14. E. Chipumuro, E. Marco, C. L. Christensen, N. Kwiatkowski, T. Zhang, C. M. Hatheway, B. J. Abraham, B. Sharma, C. Yeung, A. Altabef, A. Perez-Atayde, K. K. Wong, G. C. Yuan, N. S. Gray, R. A. Young, R. E. George, CDK7 inhibition suppresses super-enhancer-linked oncogenic transcription in MYCN-driven cancer. *Cell* **159**, 1126–1139 (2014).
15. C. L. Christensen, N. Kwiatkowski, B. J. Abraham, J. Carretero, F. Al-Shahrour, T. Zhang, E. Chipumuro, G. S. Herter-Sprie, E. A. Akbay, A. Altabef, J. Zhang, T. Shimamura, M. Capelletti, J. B. Reibel, J. D. Cavanaugh, P. Gao, Y. Liu, S. R. Michaelsen, H. S. Poulsen, A. R. Aref, D. A. Barbie, J. E. Bradner, R. E. George, N. S. Gray, R. A. Young, K.-K. Wong, Targeting transcriptional addictions in small cell lung cancer with a covalent CDK7 inhibitor. *Cancer Cell* **26**, 909–922 (2014).
16. Y. Wang, T. Zhang, N. Kwiatkowski, B. J. Abraham, T. I. Lee, S. Xie, H. Yuzugullu, T. von, H. Li, Z. Lin, D. G. Stover, E. Lim, Z. C. Wang, J. D. Iglehart, R. A. Young, N. S. Gray, J. J. Zhao, CDK7-dependent transcriptional addiction in triple-negative breast cancer. *Cell* **163**, 174–186 (2015).
17. Z. Zhang, H. Peng, X. Wang, X. Yin, P. Ma, Y. Jing, M.-C. Cai, J. Liu, M. Zhang, S. Zhang, K. Shi, W.-Q. Gao, W. di, G. Zhuang, Preclinical efficacy and molecular mechanism of targeting CDK7-dependent transcriptional addiction in ovarian cancer. *Mol. Cancer Ther.* **16**, 1739–1750 (2017).

18. J. E. Delmore, G. C. Issa, M. E. Lemieux, P. B. Rahl, J. Shi, H. M. Jacobs, E. Kastritis, T. Gilpatrick, R. M. Paranal, J. Qi, M. Chesi, A. C. Schinzel, M. R. McKeown, T. P. Heffernan, C. R. Vakoc, P. L. Bergsagel, I. M. Ghobrial, P. G. Richardson, R. A. Young, W. C. Hahn, K. C. Anderson, A. L. Kung, J. E. Bradner, C. S. Mitsiades, BET bromodomain inhibition as a therapeutic strategy to target c-Myc. *Cell* **146**, 904–917 (2011).
19. M. A. Dawson, R. K. Prinjha, A. Dittmann, G. Giotopoulos, M. Bantscheff, W. I. Chan, S. C. Robson, C.-W. Chung, C. Hopf, M. M. Savitski, C. Huthmacher, E. Gudgin, D. Lugo, S. Beinke, T. D. Chapman, E. J. Roberts, P. E. Soden, K. R. Auger, O. Mirguet, K. Doehner, R. Delwel, A. K. Burnett, P. Jeffrey, G. Drewes, K. Lee, B. J. P. Huntly, T. Kouzarides, Inhibition of BET recruitment to chromatin as an effective treatment for MLL-fusion leukaemia. *Nature* **478**, 529–533 (2011).
20. Z. Zhang, P. Ma, Y. Jing, Y. Yan, M.-C. Cai, M. Zhang, S. Zhang, H. Peng, Z.-L. Ji, W. di, Z. Gu, W.-Q. Gao, G. Zhuang, BET bromodomain inhibition as a therapeutic strategy in ovarian cancer by downregulating FoxM1. *Theranostics* **6**, 219–230 (2016).
21. J. Cidado, S. Boiko, T. Proia, D. Ferguson, S. W. Criscione, M. San Martin, P. Pop-Damkov, N. Su, V. N. Roamio Franklin, C. Sekhar Reddy Chilamakuri, C. S. D'Santos, W. Shao, J. C. Saeh, R. Koch, D. M. Weinstock, M. Zinda, S. E. Fawell, L. Drew, AZD4573 is a highly selective CDK9 inhibitor that suppresses MCL-1 and induces apoptosis in hematologic cancer cells. *Clin. Cancer Res.* **26**, 922–934 (2020).
22. T. Zhang, N. Kwiatkowski, C. M. Olson, S. E. Dixon-Clarke, B. J. Abraham, A. K. Greifenberg, S. B. Ficarro, J. M. Elkins, Y. Liang, N. M. Hannett, T. Manz, M. Hao, B. Bartkowiak, A. L. Greenleaf, J. A. Marto, M. Geyer, A. N. Bullock, R. A. Young, N. S. Gray, Covalent targeting of remote cysteine residues to develop CDK12 and CDK13 inhibitors. *Nat. Chem. Biol.* **12**, 876–884 (2016).
23. V. Quereda, S. Bayle, F. Vena, S. M. Frydman, A. Monastyrskyi, W. R. Roush, D. R. Duckett, Therapeutic targeting of CDK12/CDK13 in triple-negative breast cancer. *Cancer Cell* **36**, 545–558.e7 (2019).
24. L. Cheng, S. Zhou, S. Zhou, K. Shi, Y. Cheng, M.-C. Cai, K. Ye, L. Lin, Z. Zhang, C. Jia, H. Xiang, J. Zang, M. Zhang, X. Yin, Y. Li, W. di, G. Zhuang, L. Tan, Dual inhibition of CDK12/CDK13 targets both tumor and immune cells in ovarian cancer. *Cancer Res.* **82**, 3588–3602 (2022).
25. Y. Shi, D. C. di Giammartino, D. Taylor, A. Sarkeshik, W. J. Rice, J. R. Yates III, J. Frank, J. L. Manley, Molecular architecture of the human pre-mRNA 3′ processing complex. *Mol. Cell* **33**, 365–376 (2009).
26. S. Chan, E.-A. Choi, Y. Shi, Pre-mRNA 3′-end processing complex assembly and function. *Wiley Interdiscip Rev RNA* **2**, 321–335 (2011).
27. D. F. Colgan, J. L. Manley, Mechanism and regulation of mRNA polyadenylation. *Genes Dev.* **11**, 2755–2766 (1997).
28. K. Ryan, O. Calvo, J. L. Manley, Evidence that polyadenylation factor CPSF-73 is the mRNA 3′ processing endonuclease. *RNA* **10**, 565–573 (2004).
29. C. R. Mandel, S. Kaneko, H. Zhang, D. Gebauer, V. Vethantham, J. L. Manley, L. Tong, Polyadenylation factor CPSF-73 is the pre-mRNA 3′-end-processing endonuclease. *Nature* **444**, 953–956 (2006).
30. C. C. MacDonald, J. Wilusz, T. Shenk, The 64-kilodalton subunit of the CstF polyadenylation factor binds to pre-mRNAs downstream of the cleavage site and influences cleavage site location. *Mol. Cell. Biol.* **14**, 6647–6654 (1994).
31. H. de Vries, U. Rüegsegger, W. Hübner, A. Friedlein, H. Langen, W. Keller, Human pre-mRNA cleavage factor II_m contains homologs of yeast proteins and bridges two other cleavage factors. *EMBO J.* **19**, 5895–5904 (2000).
32. Y. Shi, J. L. Manley, The end of the message: Multiple protein-RNA interactions define the mRNA polyadenylation site. *Genes Dev.* **29**, 889–897 (2015).
33. S. L. Chan, I. Huppertz, C. Yao, L. Weng, J. J. Moresco, J. R. Yates III, J. Ule, J. L. Manley, Y. Shi, CPSF30 and Wdr33 directly bind to AAUAAA in mammalian mRNA 3′ processing. *Genes Dev.* **28**, 2370–2380 (2014).
34. L. Schönemann, U. Kühn, G. Martin, P. Schäfer, A. R. Gruber, W. Keller, M. Zavolan, E. Wahle, Reconstitution of CPSF active in polyadenylation: Recognition of the polyadenylation signal by WDR33. *Genes Dev.* **28**, 2381–2393 (2014).
35. Y. Sun, Y. Zhang, K. Hamilton, J. L. Manley, Y. Shi, T. Walz, L. Tong, Molecular basis for the recognition of the human AAUAAA polyadenylation signal. *Proc. Natl. Acad. Sci. U.S.A.* **115**, E1419–E1428 (2018).
36. S. Helmling, A. Zhelkovsky, C. L. Moore, Fip1 regulates the activity of poly(A) polymerase through multiple interactions. *Mol. Cell. Biol.* **21**, 2026–2037 (2001).
37. I. Kaufmann, G. Martin, A. Friedlein, H. Langen, W. Keller, Human Fip1 is a subunit of CPSF that binds to U-rich RNA elements and stimulates poly(A) polymerase. *EMBO J.* **23**, 616–626 (2004).
38. N. G. Kolev, T. A. Yario, E. Benson, J. A. Steitz, Conserved motifs in both CPSF73 and CPSF100 are required to assemble the active endonuclease for histone mRNA 3′-end maturation. *EMBO Rep.* **9**, 1013–1018 (2008).
39. Y. Zhang, Y. Sun, Y. Shi, T. Walz, L. Tong, Structural insights into the human pre-mRNA 3′-end processing machinery. *Mol. Cell* **77**, 800–809.e6 (2020).
40. C. H. Hill, V. Boreikaitė, A. Kumar, A. Casañal, P. Kubík, G. Degliesposti, S. Maslen, A. Mariani, O. von Loeffelholz, M. Girbig, M. Skehel, L. A. Passmore, Activation of the endonuclease that defines mRNA 3′ ends requires incorporation into an 8-subunit core cleavage and polyadenylation factor complex. *Mol. Cell* **73**, 1217–1231.e11 (2019).
41. P. C. Stirling, Y. A. Chan, S. W. Minaker, M. J. Aristizabal, I. Barrett, P. Sipahimalani, M. S. Kobor, P. Hieter, R-loop-mediated genome instability in mRNA cleavage and polyadenylation mutants. *Genes Dev.* **26**, 163–175 (2012).
42. F. Teloni, J. Michelena, A. Lezaja, S. Kilic, C. Ambrosi, S. Menon, J. Dobrovolna, R. Imhof, P. Janscak, T. Baubec, M. Altmeyer, Efficient pre-mRNA cleavage prevents replication-stress-associated genome instability. *Mol. Cell* **73**, 670–683.e12 (2019).
43. C. Haag, D. Stadel, S. Zhou, M. G. Bachem, P. Moller, K. M. Debatin, S. Fulda, Identification of c-FLIP(L) and c-FLIP(S) as critical regulators of death receptor-induced apoptosis in pancreatic cancer cells. *Gut* **60**, 225–237 (2011).
44. K. Wang, H.-M. Yu, Z.-H. Liu, Y.-J. Xiang, J.-Y. Zhong, Q.-Z. Ni, L.-P. Zhou, C. Liang, H.-K. Zhou, W.-W. Pan, W.-X. Guo, J. Shi, S.-Q. Cheng, Efficacy and safety of a triple combination of atezolizumab, bevacizumab plus GEMOX for advanced biliary tract cancer: A multicenter, single-arm, retrospective study. *Therap. Adv. Gastroenterol.* **16**, 17562848231160630 (2023).
45. S. Braig, A.-K. Bosserhoff, Death inducer-obliterator 1 (Dido1) is a BMP target gene and promotes BMP-induced melanoma progression. *Oncogene* **32**, 837–848 (2013).
46. T. Ohira, H. Kojima, Y. Kuroda, S. Aoki, D. Inaoka, M. Osaki, H. Wanibuchi, F. Okada, M. Oshimura, H. Kugoh, PITX1 protein interacts with ZCCHC10 to regulate hTERT mRNA transcription. *PLOS ONE* **14**, e0217605 (2019).
47. K. Shi, X. Yin, M.-C. Cai, Y. Yan, C. Jia, P. Ma, S. Zhang, Z. Zhang, Z. Gu, M. Zhang, W. di, G. Zhuang, PAX8 regulon in human ovarian cancer links lineage dependency with epigenetic vulnerability to HDAC inhibitors. *eLife* **8**, e44306 (2019).
48. Y. Qiao, J. Chen, Y. B. Lim, M. L. Finch-Edmondson, V. P. Seshachalam, L. Qin, T. Jiang, B. C. Low, H. Singh, C. T. Lim, M. Sudol, YAP regulates actin dynamics through ARHGAP29 and promotes metastasis. *Cell Rep.* **19**, 1495–1502 (2017).
49. C. He, X. Lv, G. Hua, S. M. Lele, S. Remmenga, J. Dong, J. S. Davis, C. Wang, YAP forms autocrine loops with the ERBB pathway to regulate ovarian cancer initiation and progression. *Oncogene* **34**, 6040–6054 (2015).
50. T. A. Knijnenburg, L. Wang, M. T. Zimmermann, N. Chambwe, G. F. Gao, A. D. Cherniack, H. Fan, H. Shen, G. P. Way, C. S. Greene, Y. Liu, R. Akbani, B. Feng, L. A. Donehower, C. Miller, Y. Shen, M. Karimi, H. Chen, P. Kim, P. Jia, E. Shinbrot, S. Zhang, J. Liu, H. Hu, M. H. Bailey, C. Yau, D. Wolf, Z. Zhao, J. N. Weinstein, L. Li, L. Ding, G. B. Mills, P. W. Laird, D. A. Wheeler, I. Shmulevich; The Cancer Genome Atlas Research Network, R. J. Monnat Jr., Y. Xiao, C. Wang, Genomic and molecular landscape of DNA damage repair deficiency across the cancer genome atlas. *Cell Rep.* **23**, 239–254.e6 (2018).
51. E. Sonoiki, C. L. Ng, M. C. S. Lee, D. Guo, Y. K. Zhang, Y. Zhou, M. R. K. Alley, V. Ahyong, L. M. Sanz, M. J. Lafuente-Monasterio, C. Dong, P. G. Schupp, J. Gut, J. Legac, R. A. Cooper, F.-J. Gamo, J. DeRisi, Y. R. Freund, D. A. Fidock, P. J. Rosenthal, A potent antimalarial benzoxaborole targets a *Plasmodium falciparum* cleavage and polyadenylation specificity factor homologue. *Nat. Commun.* **8**, 14574 (2017).
52. A. Palencia, A. Bougdour, M. P. Brenier-Pinchart, B. Touquet, R. L. Bertini, C. Sensi, G. Gay, J. Vollaire, V. Josserand, E. Easom, Y. R. Freund, H. Pelloux, P. J. Rosenthal, S. Cusack, M.-A. Hakimi, Targeting toxoplasma gondii CPSF3 as a new approach to control toxoplasmosis. *EMBO Mol. Med.* **9**, 385–394 (2017).
53. R. J. Wall, E. Rico, I. Lukac, F. Zuccotto, S. Elg, I. H. Gilbert, Y. Freund, M. R. K. Alley, M. C. Field, S. Wyllie, D. Horn, Clinical and veterinary trypanocidal benzoxaboroles target CPSF3. *Proc. Natl. Acad. Sci. U.S.A.* **115**, 9616–9621 (2018).
54. C. Swale, A. Bougdour, A. Gnahoui-David, J. Tottey, S. Georgeault, F. Laurent, A. Palencia, M.-A. Hakimi, Metal-captured inhibition of pre-mRNA processing activity by CPSF3 controls Cryptosporidium infection. *Sci. Transl. Med.* **11**, eaax7161 (2019).
55. N. T. Ross, F. Lohmann, S. Carbonneau, A. Fazal, W. A. Weihofen, S. Gleim, M. Salcius, F. Sigoillot, M. Henault, S. H. Carl, J. B. Rodríguez-Molina, H. R. Miller, S. M. Brittain, J. Murphy, M. Zambrowski, G. Boynton, Y. Wang, A. Chen, G. J. Molind, J. H. Wilbertz, C. G. Artus-Revel, M. Jia, F. A. Akinjiyan, J. Turner, J. Knehr, W. Carbone, S. Schuierer, J. S. Reece-Hoyes, K. Xie, C. Saran, E. T. Williams, G. Roma, M. Spencer, J. Jenkins, E. L. George, J. R. Thomas, G. Michaud, M. Schirle, J. Tallarico, L. A. Passmore, J. A. Chao, R. E. J. Beckwith, CPSF3-dependent pre-mRNA processing as a druggable node in AML and Ewing's sarcoma. *Nat. Chem. Biol.* **16**, 50–59 (2020).
56. J. Zhang, J. Zhang, G. Hao, W. Xin, F. Yang, M. Zhu, H. Zhou, Design, synthesis, and structure-activity relationship of 7-propanamide benzoxaboroles as potent anticancer agents. *J. Med. Chem.* **62**, 6765–6784 (2019).
57. T. J. Gonda, R. G. Ramsay, Directly targeting transcriptional dysregulation in cancer. *Nat. Rev. Cancer* **15**, 686–694 (2015).
58. S. J. Vervoort, J. R. Devlin, N. Kwiatkowski, M. Teng, N. S. Gray, R. W. Johnstone, Targeting transcription cycles in cancer. *Nat. Rev. Cancer* **22**, 5–24 (2022).

59. R. Sandberg, J. R. Neilson, A. Sarma, P. A. Sharp, C. B. Burge, Proliferating cells express mRNAs with shortened 3′ untranslated regions and fewer microRNA target sites. *Science* **320**, 1643–1647 (2008).
60. C. Mayr, D. P. Bartel, Widespread shortening of 3′UTRs by alternative cleavage and polyadenylation activates oncogenes in cancer cells. *Cell* **138**, 673–684 (2009).
61. Y. Xiang, Y. Ye, Y. Lou, Y. Yang, C. Cai, Z. Zhang, T. Mills, N.-Y. Chen, Y. Kim, F. Muge Ozguc, L. Diao, H. Karmouty-Quintana, Y. Xia, R. E. Kellems, Z. Chen, M. R. Blackburn, S.-H. Yoo, A. B. Shyu, G. B. Mills, L. Han, Comprehensive characterization of alternative polyadenylation in human cancer. *J. Natl. Cancer Inst.* **110**, 379–389 (2018).
62. Z. Xia, L. A. Donehower, T. A. Cooper, J. R. Neilson, D. A. Wheeler, E. J. Wagner, W. Li, Dynamic analyses of alternative polyadenylation from RNA-seq reveal a 3′-UTR landscape across seven tumour types. *Nat. Commun.* **5**, 5274 (2014).
63. C. P. Masamha, Z. Xia, J. Yang, T. R. Albrecht, M. Li, A.-B. Shyu, W. Li, E. J. Wagner, CFIm25 links alternative polyadenylation to glioblastoma tumour suppression. *Nature* **510**, 412–416 (2014).
64. A. Ogorodnikov, M. Levin, S. Tattikota, S. Tokalov, M. Hoque, D. Scherzinger, F. Marini, A. Poetsch, H. Binder, S. Macher-Göppinger, H. C. Probst, B. Tian, M. Schaefer, K. J. Lackner, F. Westermann, S. Danckwardt, Transcriptome 3′end organization by PCF11 links alternative polyadenylation to formation and neuronal differentiation of neuroblastoma. *Nat. Commun.* **9**, 5331 (2018).
65. M. Clerici, M. Faini, R. Aebersold, M. Jinek, Structural insights into the assembly and polyA signal recognition mechanism of the human CPSF complex. *eLife* **6**, e33111 (2017).
66. M. Clerici, M. Faini, L. M. Muckenfuss, R. Aebersold, M. Jinek, Structural basis of AAUAAA polyadenylation signal recognition by the human CPSF complex. *Nat. Struct. Mol. Biol.* **25**, 135–138 (2018).
67. B. R. Sabari, A. Dall'Agnese, A. Boija, I. A. Klein, E. L. Coffey, K. Shrinivas, B. J. Abraham, N. M. Hannett, A. V. Zamudio, J. C. Manteiga, C. H. Li, Y. E. Guo, D. S. Day, J. Schuijers, E. Vasile, S. Malik, D. Hnisz, T. I. Lee, I. I. Cisse, R. G. Roeder, P. A. Sharp, A. K. Chakraborty, R. A. Young, Coactivator condensation at super-enhancers links phase separation and gene control. *Science* **361**, eaar3958 (2018).
68. A. Boija, I. A. Klein, B. R. Sabari, A. Dall'Agnese, E. L. Coffey, A. V. Zamudio, C. H. Li, K. Shrinivas, J. C. Manteiga, N. M. Hannett, B. J. Abraham, L. K. Afeyan, Y. E. Guo, J. K. Rimel, C. B. Fant, J. Schuijers, T. I. Lee, D. J. Taatjes, R. A. Young, Transcription factors activate genes through the phase-separation capacity of their activation domains. *Cell* **175**, 1842–1855. e16 (2018).
69. W.-K. Cho, J. H. Spille, M. Hecht, C. Lee, C. Li, V. Grube, I. I. Cisse, Mediator and RNA polymerase II clusters associate in transcription-dependent condensates. *Science* **361**, 412–415 (2018).
70. H. Lu, D. Yu, A. S. Hansen, S. Ganguly, R. Liu, A. Heckert, X. Darzacq, Q. Zhou, Phase-separation mechanism for C-terminal hyperphosphorylation of RNA polymerase II. *Nature* **558**, 318–323 (2018).
71. P. A. Gutierrez, K. Baughman, Y. Sun, L. Tong, A real-time fluorescence assay for CPSF73, the nuclease for pre-mRNA 3′-end processing. *RNA* **27**, 1148–1154 (2021).
72. S. J. Dubbury, P. L. Boutz, P. A. Sharp, CDK12 regulates DNA repair genes by suppressing intronic polyadenylation. *Nature* **564**, 141–145 (2018).
73. M. Krajewska, R. Dries, A. V. Grassetti, S. Dust, Y. Gao, H. Huang, B. Sharma, D. S. Day, N. Kwiatkowski, M. Pomaville, O. Dodd, E. Chipumuro, T. Zhang, A. L. Greenleaf, G. C. Yuan, N. S. Gray, R. A. Young, M. Geyer, S. A. Gerber, R. E. George, CDK12 loss in cancer cells affects DNA damage response genes through premature cleavage and polyadenylation. *Nat. Commun.* **10**, 1757 (2019).
74. P. M. Joshi, S. L. Sutor, C. J. Huntoon, L. M. Karnitz, Ovarian cancer-associated mutations disable catalytic activity of CDK12, a kinase that promotes homologous recombination repair and resistance to cisplatin and poly(ADP-ribose) polymerase inhibitors. *J. Biol. Chem.* **289**, 9247–9253 (2014).
75. H. Li, R. Durbin, Fast and accurate short read alignment with Burrows-Wheeler transform. *Bioinformatics* **25**, 1754–1760 (2009).
76. H. Li, B. Handsaker, A. Wysoker, T. Fennell, J. Ruan, N. Homer, G. Marth, G. Abecasis, R. Durbin; 1000 Genome Project Data Processing Subgroup, The sequence alignment/map format and SAMtools. *Bioinformatics (Oxford, England)* **25**, 2078–2079 (2009).
77. V. Boeva, T. Popova, K. Bleakley, P. Chiche, J. Cappo, G. Schleiermacher, I. Janoueix-Lerosey, O. Delattre, E. Barillot, Control-FREEC: A tool for assessing copy number and allelic content using next-generation sequencing data. *Bioinformatics* **28**, 423–425 (2012).
78. B. Langmead, S. L. Salzberg, Fast gapped-read alignment with Bowtie 2. *Nat. Methods* **9**, 357–359 (2012).
79. D. Kim, J. M. Paggi, C. Park, C. Bennett, S. L. Salzberg, Graph-based genome alignment and genotyping with HISAT2 and HISAT-genotype. *Nat. Biotechnol.* **37**, 907–915 (2019).
80. Y. Liao, G. K. Smyth, W. Shi, featureCounts: An efficient general purpose program for assigning sequence reads to genomic features. *Bioinformatics* **30**, 923–930 (2014).
81. M. I. Love, W. Huber, S. Anders, Moderated estimation of fold change and dispersion for RNA-seq data with DESeq2. *Genome Biol.* **15**, 550 (2014).
82. L. Li, K.-L. Huang, Y. Gao, Y. Cui, G. Wang, N. D. Elrod, Y. Li, Y. E. Chen, P. Ji, F. Peng, W. K. Russell, E. J. Wagner, W. Li, An atlas of alternative polyadenylation quantitative trait loci contributing to complex trait and disease heritability. *Nat. Genet.* **53**, 994–1005 (2021).
83. Z. Zhao, Q. Xu, R. Wei, L. Huang, W. Wang, G. Wei, T. Ni, Comprehensive characterization of somatic variants associated with intronic polyadenylation in human cancers. *Nucleic Acids Res.* **49**, 10369–10381 (2021).
84. A. Butler, P. Hoffman, P. Smibert, E. Papalexi, R. Satija, Integrating single-cell transcriptomic data across different conditions, technologies, and species. *Nat. Biotechnol.* **36**, 411–420 (2018).
85. J. D. Buenrostro, P. G. Giresi, L. C. Zaba, H. Y. Chang, W. J. Greenleaf, Transposition of native chromatin for fast and sensitive epigenomic profiling of open chromatin, DNA-binding proteins and nucleosome position. *Nat. Methods* **10**, 1213–1218 (2013).
86. Y. Zhang, T. Liu, C. A. Meyer, J. Eeckhoute, D. S. Johnson, B. E. Bernstein, C. Nusbaum, R. M. Myers, M. Brown, W. Li, X. S. Liu, Model-based Analysis of ChIP-seq (MACS). *Genome Biol.* **9**, R137 (2008).
87. P. Anees, S. Sreejith, A. Ajayaghosh, Self-assembled near-infrared dye nanoparticles as a selective protein sensor by activation of a dormant fluorophore. *J. Am. Chem. Soc.* **136**, 13233–13239 (2014).

Acknowledgments: We would like to thank Y. Sun from ShanghaiTech University for technical support and all laboratory members for helpful discussions. **Funding:** This work was supported by the National Natural Science Foundation of China (82203271 to P.S.; 82172596 and 82373351 to G.Z.; 21837004 and 82151212 to L.T.; 81972429 and 82273388 to R.Z.; 81974454 to W.D.; 82173077 and 82211540402 to X.Y.; 82173242 to T.S.; 82022078 to L.W.T.C.; and 82173111 to M. Z.), Shanghai Municipal Education Commission-Gaofeng Clinical Medicine Grant Support (20161313 to G.Z.), innovative research team of high-level local universities in Shanghai (SHSMU-ZLCX20210200 to G.Z.), 111project (no. B21024 to G.Z.), the Strategic Priority Research Program of the Chinese Academy of Sciences (XDB39050500 to L.T.), and Shanghai Municipal Science and Technology Major Project (grant no.2019SHZDZX02 to L.T.). **Author contributions:** Conceptualization: G.Z., L.T., R.Z., and W.D. Methodology: P.S., K.Y., H.X., Q.H., X. Z., C.Q., and M.Z. Data analyses: M.-C.C., J.C., Y.S., and L.L. Investigation: P.S., K.Y., H.X., Z.Z., Q.H., and X.Z. Supervision: G.Z., L.T., L.W.T.C., and T.S. Writing—original draft: P.S., K.Y., H.X., and X.Z. Writing—review and editing: G.Z. and L.T. Project administration: G.Z., X.Y., and Y.L. **Competing interests:** The authors declare that they have no competing interests. **Data and materials availability:** All data needed to evaluate the conclusions in the paper are present in the paper and/or the Supplementary Materials. The sequencing data have been deposited in the NCBI BioProject database under the accession number PRJNA892709.

Submitted 1 June 2023
Accepted 19 October 2023
Published 22 November 2023
10.1126/sciadv.adj0123